Sodium Ion Microscale Electrochemical Energy Storage Device: Present Status and Future Perspective

*Jiaxin Ma, Shuanghao Zheng, Pratteek Das, Pengfei Lu, Yan Yu,**
*and Zhong-Shuai Wu**

The unprecedented development of flexible, wearable, and miniaturized electronics has envisaged a glorious future for mankind. However, at the same time, it has escalated the demand for microscale electrochemical energy storage devices (MEESDs). With abundant resources, low cost and properties similar to lithium, sodium ion MEESDs (NIMEESDs), e.g., sodium ion microcapacitors (NIMCs) and microbatteries (NIMBs), have emerged as high-performance and competitive candidates for effectively powering microelectronics. Herein, the state-of-the-art advances and recent developments in designing high-performance NIMEESDs are reviewed. The study begins by introducing NIMEESDs, focusing on distinct device configurations, including stacked, interdigital, fiber-shaped, and 3D geometries. Subsequently, the recent achievements of various well-designed microelectrodes in Na ion storage covering intercalation, conversion, and alloying-type reaction mechanisms are systematically discussed. Based on the device architecture, the status of high-power and high-energy NIMCs and NIMBs is presented. More attention is paid to the exceptional flexibility, aesthetic versatility, shape diversity, and tailored integration of NIMEESDs. Finally, future challenges associated with NIMEESDs and corresponding prospects are discussed from the viewpoint of electrochemical active materials, electrode structure, microfabrication process, and self-powered integrated microsystems.

1. Introduction

With the onset of "intelligent" era marked by flexible and wearable microelectronics, the Internet of Things (IoT), implantable medical devices, smart sensors, and wireless charging,[1–4] conventional electrochemical energy storage devices (EESDs) being bulky and rigid cannot meet the demand of rising microelectronics due to poor integrability.[5–7] In addition, conventional EESDs also have severe problems stemming from intrinsic limitation on architecture, for instance, thick commercial separator (glass fiber) limiting the ion diffusion kinetics, and the safety issue of commercial batteries pertaining to the alkali metals (e.g., Li, Na).[8,9] Naturally, their electrochemical performance is subpar and cannot keep up with the development of shapeless and flexible integrated circuits.[10–13] These issues have intensified the pursuit of flexible, versatile, compatible, and on-chip microscale EESDs (MEESDs) as promising power source, which could be integrated with microrobots, wearable devices, or microelectronics with low power consumption (milliwatts to nanowatts).[14–17] Microsupercapacitors (MSCs) with high power density, fast charge–discharge rate and ultra-long life have exhibited easy integration, and good mechanical flexibility,[18,19] which store charge by fast ion adsorption/desorption or highly reversible redox reactions at the interface between the electrode and electrolyte.[20,21] MSCs can power various electronics from watts to microwatts power (**Figure 1**), but the energy density of MSCs is insufficient to support the high-energy consumption electronics, such as long-range communication, and cannot provide power supply for a long time (hours).[22,23] By contrast, microbatteries (MBs) with high energy density could be hopeful to satisfy the energy requirements of some mobile devices for long-term consumption from nanowatts to milliwatts, such as 32 KHz quartz oscillator in nanowatts, electronic watch in microwatts, and miniature

J. Ma, Dr. S. Zheng, P. Das, Dr. P. Lu, Prof. Z.-S. Wu
State Key Laboratory of Catalysis
Dalian Institute of Chemical Physics
Chinese Academy of Sciences
457 Zhongshan Road, Dalian 116023, China
E-mail: wuzs@dicp.ac.cn

J. Ma, P. Das
University of Chinese Academy of Sciences
19 A Yuquan Road, Shijingshan District, Beijing 100049, China

The ORCID identification number(s) for the author(s) of this article can be found under https://doi.org/10.1002/sstr.202000053.

DOI: 10.1002/sstr.202000053

Dr. S. Zheng, Prof. Y. Yu, Prof. Z.-S. Wu
Dalian National Laboratory for Clean Energy
Chinese Academy of Sciences
457 Zhongshan Road, Dalian 116023, China
E-mail: yanyumse@ustc.edu.cn

Prof. Y. Yu
Hefei National Laboratory for Physical Sciences at the Microscale
Department of Materials Science and Engineering
CAS Key Laboratory of Materials for Energy Conversion
University of Science and Technology of China
Hefei, Anhui 230026, China

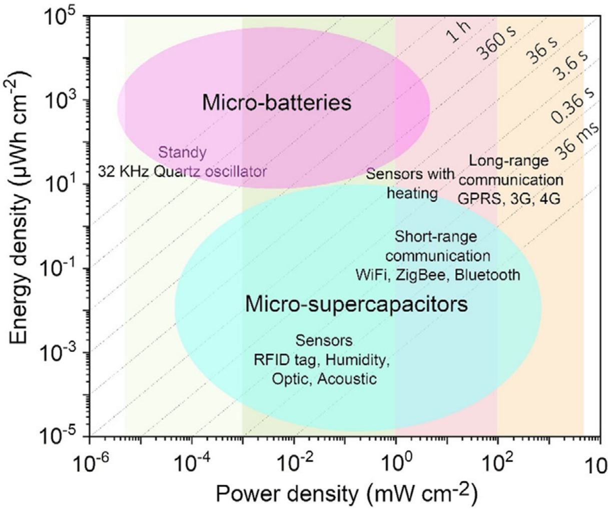

Figure 1. Ragone plot of the state-of-the-art MSCs and MBs. The vertical shaded areas show various electronics with different power consumption.

frequency modulation receiver in milliwatts.[24,25] However, the higher power supply above tens of watts cannot be replied on the MBs with sluggish kinetics. Therefore, it is feasible to combine high-power MSCs and high-energy MBs together or develop hybrid ion microcapacitors in terms of specific application scenarios of electronic microsystems.

So far, lithium ion MEESDs, e.g., lithium ion MBs (LIMBs) and lithium ion microcapacitors (LIMCs),[26–28] have provided feasible strategies to meet microelectronic power demands with desired electrochemical performance due to the distinguished physical properties, such as the lowest standard potential, smallest Stokes radii, highest theoretical capacity, and charge-to-mass ratio of Li ions (**Table 1**). Although LIMBs have high energy density, they suffer from low power density. This was mitigated to some extent by LIMCs that combine high capacity of battery materials and fast charge–discharge of capacitive materials, inheriting the advantages of MBs with high energy density and MSCs with high power density.[27,28] However, considering the rapidly depleting reserves of lithium in the crust ($<$20 ppm), the increasingly high price of lithium resources, and uneven distribution (mainly in South America), it is necessary to develop novel candidates to replace lithium ion MEESDs.[29,30]

Other alkali metals (Na, K) and bivalent metals (Mg, Ca) have obtained wide research interest attributed to the elemental abundance. Importantly, Na ions exhibit a weaker interaction with solvent and a smaller solvation shell with a hydrated ionic radius (1.84 Å) in comparison with Li^+ (2.38 Å), Mg^{2+} (3.47 Å), Ca^{2+} (3.10 Å), and Zn^{2+} (3.49 Å) ions.[31,32] Consequently, the Na ions show faster diffusion kinetics, leading to high-power sodium ion MEESDs (NIMEESDs) with fast charge–discharge rate.[33] Furthermore, based on the Faraday's law of electrolysis, a high charge-to-mass ratio of ions is beneficial for a high gravimetric capacity.[34,35] NIMEESDs are a possible alternative to lithium-based batteries, owing to its considerable charge-to-mass ratio and elemental abundance compared with K ions. In addition, Al current collector exhibits thermodynamical stability with Na ions in low potential and can be simultaneously used in both anode and cathode, which is advantageous to reduce the cost of sodium ion batteries (NIBs).[36–39] Generally, NIMEESDs are classified into sodium ion MBs (NIMBs) and sodium ion microcapacitors (NIMCs) considering the storage mechanisms.[40] The former delivers high energy density by redox reactions of bulk electrode involving three major reaction mechanisms, i.e., intercalation,[29,41,42] conversion,[9,43,44] and alloying type.[45,46] NIMCs consisting of a battery-type material and a capacitive-type material can store energy by Na ion insertion/extraction in the anode bulk and anion adsorption/desorption at the cathode surface.[47] Therefore, it is obvious that NIMCs also inherit the role of LIMCs and bridge the gap between MBs and MSCs.

Herein, we begin with a brief introduction of MEESDs from the concept definition to device configurations. Second, we elaborate Na ion storage mechanisms in electrode materials, outlining their superiorities and shortcomings as microelectrodes in NIMEESDs. Third, we present the recent advances of NIMEESDs with various device structures, and typically including the design, fabrication, and electrochemical performance of 2D stacked NIMCs and NIMBs, 2D in-plane interdigital NIMEESDs with exceptional integration and flexibility, as well as fiber-shaped NIMBs with distinct 1D configuration. Finally, we highlight the major challenges and future perspective of NIMEESDs.

Table 1. Comparison of the physical properties of monovalent/multivalent metal ions as charge carriers for rechargeable batteries. PC, propylene carbonate.

Physical properties	Li^+	Na^+	K^+	Mg^{2+}	Zn^{2+}	Ca^{2+}
Elemental abundance [ppm]	19.92	23601.8	23654.8	20851.2	71.43	41077.6
Relative atomic mass	6.94	23.00	39.10	24.31	65.41	40.08
Mass-to-charge ratio	6.94	23.00	39.10	12.16	32.70	20.04
Standard potential [V vs SHE]	−3.04	−2.71	−2.93	−2.4	−0.76	−2.9
Shannon's ionic radii [Å][146]	0.76	1.02	1.38	0.72	0.75	1.0
Stokes radii in water [Å][147]	2.38	1.84	1.25	3.47	3.49	3.10
Stokes radii in PC [Å][148]	4.8	4.6	3.6	–	–	–
Desolvation energy in PC [kJ mol^{-1}][33]	218.0	157.3	119.2	572.3	–	–
Specific capacity [mAh g^{-1}]	3806	1166	685	2206	820	1337
Capacity density [mAh cm^{-3}]	2061	1129	610	3834	5855	2072

2. Configuration of NIMEESDs

Even today, there is no clear definition of MEESD. In general, a MEESD is eligible to be regarded as a microdevice if it has a full footprint area limited in scale to square millimeter and electrode not more than 10 μm thick. The arrays of microelectrodes should be limited to microscale size in at least two dimensions. Devices with 3D geometries should lie within 1–10 mm^3.[48,49] In addition, the concept of MEESD can be expanded into fiber-based and free-standing thin-film electrodes.[50] Depending on the configuration of microelectrodes, NIMEESDs are classified into planar and nonplanar geometries. For planar geometry, NIMEESDs contain 2D stacked, 2D in-plane, 3D stacked, and 3D in-plane architecture.[49] 2D stacked microdevice with a sandwich structure consists of current collector, anode, cathode, and separator/electrolyte as major components (**Figure 2**a). The electrolyte ions diffuse in the vertical direction and must pass though the separator. For 2D in-plane microdevices, the cathode and anode share the same substrate, and the physical interspace between microelectrodes plays the role of separator, suggestive of ions diffusion in both horizontal and vertical direction (Figure 2b).[26,30] As the interspaces in the 2D in-plane architecture cannot be arbitrarily small, they consume a large portion of the total available area. This naturally halves the areal capacitance/capacity compared with their 2D stacked counterparts. In terms of 3D stacked microdevices, the components emerged as a 3D vertically aligned columnar-type structure (Figure 2d). Differently, 3D in-plane microdevices possess interdigital and vertical arrays of both anode and cathode on substrate (Figure 2c). Consequently, 3D microdevices not only deliver considerable areal capacitance or capacity due to the increased mass loading of active materials, but also provide higher power performance due to the multiple charge transport avenues in vertically aligned microelectrodes. It is worth mentioning that fiber-shaped microdevices can be regarded as a special class of stacked structure (Figure 2e), exhibiting unique 1D architecture with twisted, parallel, and coaxial configuration.[51–53]

3. Storage Mechanisms of NIMEESD Microelectrodes

To date, many active materials with high-performance metrics have been applied for the microelectrodes of NIMEESDs.[4,54,55] According to the reaction products and process, Na ion storage mechanisms fall into three major categories, namely, intercalation, conversion, and alloying types (**Figure 3**), similar to lithium ion storage reactions.[36] Classified by mechanisms of storage, the crucial electrochemical performance metrics of anode and cathode for NIMEESDs are shown in **Table 2**.

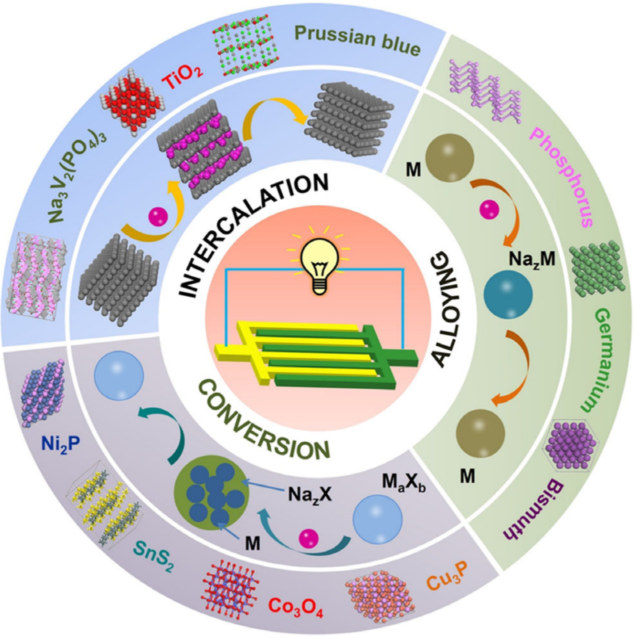

Figure 3. Schematic illustration of sodium storage materials with different reaction mechanisms of intercalation, conversion, and alloying.

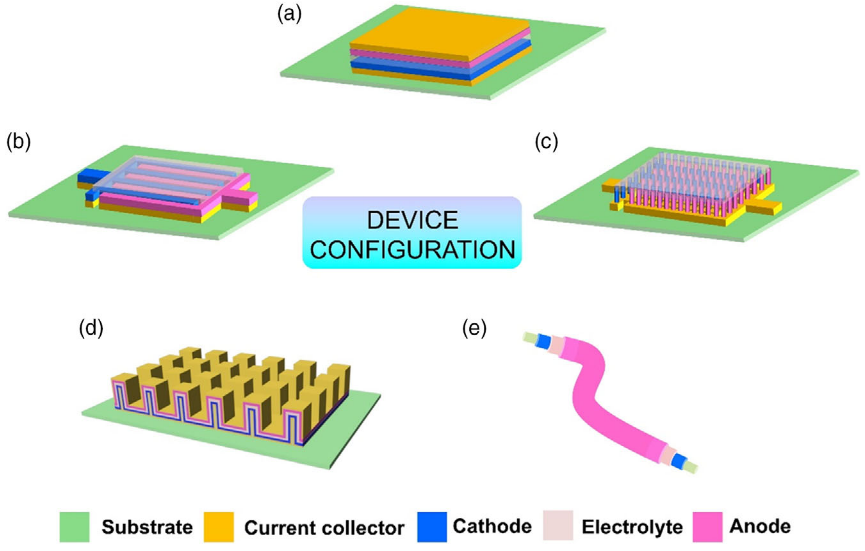

Figure 2. Schematic illustration of NIMEESDs. a) 2D stacked NIMEESDs; b) 2D in-plane NIMEESDs; c) 3D in-plane NIMEESDs; d) 3D stacked NIMEESDs; and e) fiber-shaped NIMEESDs.

Table 2. Summary of microelectrode materials for NIMEESDs. NVP@3D-NSC, NVP particles embedded in the N, S co-doped 3D porous carbon matrix; FEC, fluoroethylene carbonate; DEC, diethyl carbonate; DME, dimethyl ether.

Mechanism	Electrode	Electrolyte	Potential voltage [V] versus Na^+/Na	Specific capacity [$mAh\,g^{-1}$]	Cycle stability	Ref.
Intercalation	$NaVSnO_4$	1 M $NaClO_4$/PC	0.15–2.5	163 (0.2 C)	10 000 (84%)	[32]
	NVPF@C	1 M $NaClO_4$/EC/PC	2.0–4.3	122 (1 C)	5000 (65%)	[67]
	NVP@3D-NSC	1 M $NaClO_4$/PC/FEC	2.3–3.9	114 (1 C)	6000 (78%)	[70]
	NTO	1 M $NaClO_4$/EC/DEC/FEC	0.01–2.5	173.4 (50 mA g^{-1})	1100 (80%)	[62]
	NTO@RHCS	1 M $NaClO_4$/EC/PC/FEC	0.01–2.5	152.69 (1 C)	–	[60]
Conversion	WS_2/CNT-rGO	1 M $NaPF_6$/EC/DEC/FEC	0.01–3.0	311.4 (100 mA g^{-1})	–	[93]
	NiO/graphene	1 M $NaPF_4$/EC/DEC/FEC	0.01–3.0	629 (0.1 C)	–	[95]
	CPNW	1 M $NaClO_4$/EC/DMC/FEC	0.01–2.5	349 (50 mA g^{-1})	260 (70%)	[96]
Alloying	RP@PMCNFs	1 M $NaClO_4$/EC/DMC/FEC	0.001–2.0	1580 (100 mA g^{-1})	–	[106]
	Sn NDs@PNC	1 M $NaClO_4$/PC	0.01–2.0	633 (200 mA g^{-1})	1300 (90%)	[107]
	C@P/GA	1 M $NaClO_4$/EC/DEC/FEC	0.01–2.0	2042.5 (0.1 C)	200 (66.9%)	[108]
	Bi@3DGFs	1 M $NaPF_6$/DME	0.1–1.8	241 (0.1 A g^{-1})	2000 (92%)	[149]
Hybrid energy storage mechanisms	V_5S_8–Graphite	1 M $NaClO_4$/PC	0.01–3.0	902 (0.1 A g^{-1})	–	[111]
	Bi@Graphite	1 M $NaPF_6$/DME	0.01–1.8	160 (1 C)	10 000 (90%)	[112]
	NTO–VS_2	1 M $NaClO_4$/EC/PC/FEC	0.01–2.5	575 (0.1 C)	–	[113]

3.1. Intercalation-Type Microelectrodes

Intercalation-type microelectrodes involve the insertion/extraction of Na ions into/from electrode bulk during discharge/charge process, in which the guest Na ions intercalate into the hosts with negligible or rather small volume change. Typically, carbon materials are suitable intercalation materials as anodes for NIMEESDs on account of their stable structure, chemical stability, and cost-effectiveness. In view of Na ions' larger radius than Li ions, graphite with interlayer spacing of 0.335 nm cannot accommodate considerable amount of Na ions, resulting in low capacity. Therefore, disordered carbon with larger interlayer spacing is preferred for Na ion storage.[56] For example, the hierarchical porous biomass (peat moss)-derived carbon nanosheet delivered capacity of 298 $mAh\,g^{-1}$ at 50 $mA\,g^{-1}$, in which the expanded interlayer space of 0.388 nm allows the intercalation of Na ions into hierarchical micro- and mesoporosity of carbon sheet framework.[57] However, high surface area of carbonaceous materials usually leads to low initial Coulombic efficiency (ICE) (less than 50%). To tackle this issue, Yu et al. developed a freestanding film based on 3D interconnected carbon nanofibers with well-designed pore structure, interlayer spacing, and oxygen content, delivering exceptional ICE of 93% and ultra-long lifespan under a low voltage plateau of less than 0.2 V.[58] In addition, titanium-based oxides as intercalation-type anode have shown enormous potential in Na ion storage in terms of prominent capacity, exceptional cycle life, excellent rate performance, and low average Na ion insertion potential. This has been enabled by the robust structure and tiny strain during continuous intercalation/deintercalation process.[59] Typically, layered $Na_2Ti_3O_7$ (NTO) has low intercalation potential of 0.3 V and yields high energy density for NIBs.[60] For instance, low sodium-containing phase Na(1)-[Ti_3O_7] nanosheets exfoliated from layered NTO maintained capacity of 200 $mAh\,g^{-1}$.[61] These nanosheets formed by top-down approach accelerated the Na ions diffusion kinetics and also promoted the wettability of microelectrodes. Similarly, a 3D flower-like structure constructed by NTO nanosheet exhibited excellent rate performance with satisfactory capacity of 73.8 $mAh\,g^{-1}$ even at 800 $mA\,g^{-1}$. The high specific surface area of microflower structure shortened ionic diffusion pathways and strengthened the transport kinetics of electrons.[62] In addition to morphology modulation, heteroatom doping may also help tune the electrochemical activity of electrode materials. For example, sulfur-doped double-shell NTO microspheres built from 2D ultrathin nanosheets continued to deliver 162 $mAh\,g^{-1}$ after 15 000 cycles. The synergistic effects between the unique double-shell architecture with affluent open space and sulfur doping for enhancing electrical conductivity by narrowing the bandgap were responsible for this boost.[59] These results clearly show that the evolution of structure and morphology has a great influence on the improvement of electrode performance, originating from the optimized Na ion guests with tuned electrochemical activity.

For cathode materials, polyanionic compounds, Prussian blue and their derivatives have garnered much attention due to low lattice strain, considerable theoretical specific capacity, high Na ions conductivity, and moderate cyclability.[37,63–65] Polyanionic compounds largely involve olivine-type $NaFePO_4$, NASICON-type $Na_3V_2(PO_4)_3$ (NVP), and $Na_3V_2(PO_4)_2F_3$ (NVPF). The olivine-type $NaFePO_4$ cathode has high theoretical specific capacity (154 $mAh\,g^{-1}$), in which FeO_6 octahedra shares the edges and Na ions located at tetrahedral sites share the corners with PO_4 tetrahedra.[29] The vanadium-based NVP can function as both cathode with V^{3+}/V^{4+} redox process at high flat voltage plateaued at 3.3 V and anode with V^{2+}/V^{3+} redox reaction at around 1.5 V accompanying with Na ions intercalation/deintercalation, holding excellent structural stability, reversibility, and high Na ion conductivity.[29,66] Importantly, NVPF made up of VO_4F_2 octahedra and PO_4 tetrahedra delivers reversible theoretical specific of 128 mAh g^{-1} with two voltage plateaus at 3.6 and 4.1 V,[67] favorable for the construction of high-energy full NIMEESD with higher operating voltage and specific capacity.[68]

Although the robust structural stability of aforementioned electrodes readily enables long life of NIMEESDs, intrinsically poor electrical conductivity of noncarbon-based materials has adverse effect on rate capability of microdevices, especially detrimental for high power output. It is possible to overcome this issue by introducing highly conductive matrix, such as ultrathin carbon-based layers that not only support electrochemical active materials but also open abundant ion channels by structural modulation (**Figure 4**). This was evidenced in freestanding porous carbon fibers decorated by carbon-coated $Na_{3.12}Fe_{2.44}(P_2O_7)_2$ hollow spheres prepared through electrostatic spinning. The "bubble-in-nanorod" hierarchical structure provided a sort of bicontinuous electron highway and significantly enhanced electrolyte ions intercalation kinetics (Figure 4a–d),[50] which displayed lower polarization and satisfactory rate capability with capacity of 80 mAh g^{-1} at 6 C (Figure 4e,f). Another example is the stacked $Na_2Ti_3O_7$ nanosheets anchored on a unique red blood cell-like hollow carbon sphere ($Na_2Ti_3O_7$@RHCS) with enhanced conductivity and compacted density. It delivered superior capacity of ≈175.5 mAh g^{-1} at 1 C and retained a fulfilling capacity of ≈45.7 mAh g^{-1} even at 50 C (Figure 4g,h). The as-constructed structure with abundant electrochemical active sites exposed to electrolyte and improved conductivity showed smaller charge transfer resistance in comparison with pure NTO (Figure 4i).[60] In addition, Mai et al. synthesized NVP nanograins composite with 0D to 2D carbon materials, such as acetylene carbon (AC), carbon nanotubes (CNTs), and graphite nanosheets as conductive additives, respectively. The NVP/AC composite in different dimensional matrices with interconnected conductive network resulted in capacity close to theoretical value at 0.5 C and remarkable rate capability (97.0 mAh g^{-1} at 5 C).[69] Afterward, it was certified that NVP particles embedded in the matrix not only improved electrical conductivity, but also facilitated electrolyte ions transport, accounting for a higher diffusion coefficient of Na ions.[70] These results are a testimony to the effectiveness of conductive carbon matrix in remedying the sluggish reaction kinetics of intercalation-type materials during sodiation/desodiation process.

3.2. Conversion-Type Microelectrodes

Different from intercalation-type electrode, transition metal oxide (e.g., NiO, Co_3O_4, CuO, MnO, Fe_2O_3),[71–77] sulfide (e.g., SnS_2,

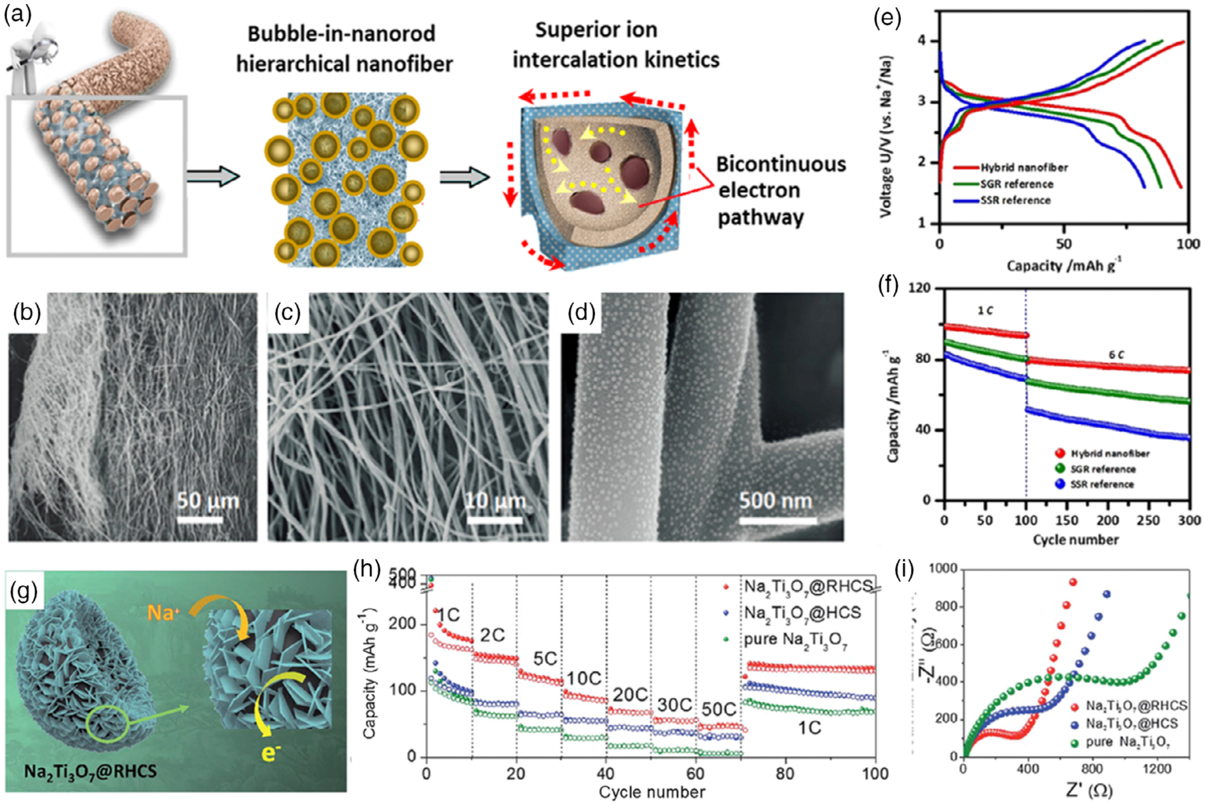

Figure 4. Intercalation-type materials in Na ions storage. a) Schematic diagram of hierarchical fiber with bicontinuous electron and ions pathways. b–d) Scanning electron microscopy (SEM) images of $Na_{3.12}Fe_{2.44}(P_2O_7)_2$ hybrid fiber with different magnifications. e) Galvanostatic charge–discharge (GCD) profiles at 1 C and f) cycling stability of $Na_{3.12}Fe_{2.44}(P_2O_7)_2$ hybrid fibers. Reproduced with permission.[50] Copyright 2018, Elsevier. g) Schematic showing the preparation process of $Na_2Ti_3O_7$@RHCS. (h) Rate capabilities and i) Nyquist plots after 5 cycles of $Na_2Ti_3O_7$@RHCS. Reproduced with permission.[60] Copyright 2018, Royal Society of Chemistry.

WS_2),[9,78] and phosphide (e.g., Ni_2P, CoP)[79,80] can form new chemical bonds and products with Na ions during charge/discharge process, which are deemed as conversion reaction materials.[81] Generally, the conversion-type materials are able to transfer multiple electrons during charging and discharging process, endowing them with higher reversible capacity.[82] For example, 2D holey Co_4S_3 nanosheets exhibited high capacity of 571 mAh g^{-1}.[83] The outstanding capacity of conversion materials is fundamental for high-performance NIMEESDs. However, there are a series of drawbacks of the conversion-type materials in Na ion storage. First, the conversion-type materials suffer from low ICE with a large irreversible capacity loss because of electrolyte decomposition that forms the solid electrolyte interphase (SEI), insufficient sodiation of conversion microelectrodes and irreversible desodiation process. For instance, SnO_2 nanocrystals dispersed on nitrogen/sulfur codoped graphene (NSGS) exhibited a low ICE of 48.4%. This hugely irreversible capacity loss will hinder the design of high-energy NIMEESDs.[7,82,84] Next, the repeated conversion reactions over multiple cycles undermine the structural stability and capacity retention of microelectrodes. For example, the capacity of CuO rapidly faded from 419 to 138 mAh g^{-1} after only 30 cycles.[85] Third, the general voltage hysteresis reduces the energy efficiency and output voltage of cells. The voltage hysteresis phenomenon is related to different Na ion mobility and increased interface of sodium compounds and transition metal derived from conversion-type microelectrode and Na metal, the asymmetrical reaction pathways during charge/discharge process, and larger polarization of conversion materials with poor conductivity.[86] For instance, the hysteresis voltage of well-designed CoSe embedded into carbon nanowires still had more than 0.4 V.[87] Importantly, the large volume expansion/shrinkage from the discrepant volume between reactants and products is extremely harmful to the structural integrity of microelectrodes, resulting in poor lifespan of microdevices and a potentially dangerous short-circuit.

To address the aforementioned problems, advanced microelectrodes with intrinsic arrays and free-standing structure are designed to uphold the structural integrity, and conductive scaffolds are embedded or coated on conversion materials to accommodate volume change and further improve Na ion kinetics (**Figure 5**).[54,88] Such freestanding electrodes can form a conductive framework without current collector or binder additives and enable high energy density of NIMEESDs.[89–91] As a representative example, cobalt phosphide (CoP) nanowires (NWs) coated by conducting polymer polypyrrole (PPy) were uniformly grown on carbon paper (CP) with strong chemical bond between active materials and conductive matrix. Benefiting from the restrained volume expansion of 1D structure and enhanced charge transfer in 3D conductive frameworks, the 1D core–shell CoP@PPy NWs/CP exhibited ultra-long cycle stability for 1000 cycles and fine rate capability.[92] Also, Yang et al. designed hierarchical aerogel based on WS_2 nanosheet and CNT-reduced graphene oxide (CNT-rGO) matrix through solvothermal and ice template-assisted method (Figure 5a,b).[93] The optimized WS_2/CNT-rGO composites with exceptional mechanical flexibility displayed remarkable rate performance with 47.2 mAh g^{-1} even at 10 000 mA g^{-1}. Importantly, after being subjected to such taxing conditions when current density was switched to 100 mA g^{-1} an excellent capacity of 342.6 mAh g^{-1} was recovered (Figure 5c).

In addition to building freestanding conductive framework, it is also feasible to fabricate 3D array microelectrodes by accommodating more accessible active materials for high energy density of NIMEESDs.[94,95] Such systems have been achieved by either growing arrays of nanowires on or engraving nanorods in metal substrates. While Yan and co-worker grew Cu_3P nanowires (CPNW) arrays (Figure 5d),[96] Zhang et al. engraved CuO nanorod arrays (CNAs) into the copper substrate.[97] Both techniques resulted in electrodes with remarkable capacity, and CPNWs showed the capacity as high as 433 mAh g^{-1} and CNAs with 640 mAh g^{-1}, strikingly close to theoretical capacity (Figure 5e). However, CNAs showed poorer ICE (68%) than CPNWs (80.6%) which might be due to more electrolyte degradation on the surface of CNAs for SEI films. The feature common to both these cases is the lack of additives and excellent volume accommodation despite repeated conversion reactions. These benefits can be further amplified by compositing oxides with conductive scaffold-like graphene as exemplified by NiO/graphene arrays that provide superb rate performance in addition to the aforementioned features.[95] To sum up, the well-designed conversion materials from the aforementioned strategies are helpful to construct ordered channels for fast ion diffusion and accommodate volume expansion, exhibiting enhanced electrochemical performance with considerable rate capability and cycle stability. These are highly favorable traits for the design of high-performance NIMEESDs.

3.3. Alloying-Type Microelectrodes

Apart from the intercalation and conversion reactions, group IVA and VA elements (Sn, Sb, Bi, Si, Ge, and P) and their intermetallic compounds participate in redox reactions with Na ions during sodiation/desodiation process, forming alloying compounds with higher capacity, such as Na_3Sb (660 mAh g^{-1}),[98] $Na_{15}Sn_4$ (847 mAh g^{-1}),[99] NaSi/$Na_{0.75}Si$ (954/725 mAh g^{-1}),[100] and Na_3P (2596 mAh g^{-1}).[101,102] These are suitable for fabricating high-energy NIMEESDs because they also exhibit low average potential range from 0.2 to 0.6 V, along with the outstanding capacity.[45] However, despite their ultrahigh capacity, large volume expansion of alloying materials with multiple intermediate phases during alloying process dramatically damages the electrode structure and corresponding interfacial contact, resulting in increased internal resistance and rapid capacity fade.[103] Moreover, the intrinsic insulating nature of alloying materials (red P [RP]: $\approx 10^{-14}$ S cm^{-1}) yields sluggish reaction kinetics, thus adverse to the desired electrochemical behavior, such as prominent Coulombic efficiency, reversible reaction process, and remarkable lifespan.[104]

To overcome the aforementioned shortcomings of alloy materials for NIMEESDs, many strategies have been proposed. These aimed to improve intrinsic weakness of alloying microelectrodes, to realize continuous conductive pathways, and to achieve satisfactory cycling stability. First, alloying-type materials were modified by encapsulating them in carbon matrix, greatly enhancing the electrical conductivity and suppressing undesirable volume expansion.[105] For instance, RP encapsulated in multichannel carbon nanofibers (RP@PMCNFs) as a freestanding microelectrode was synthesized by electrospinning and postthermal

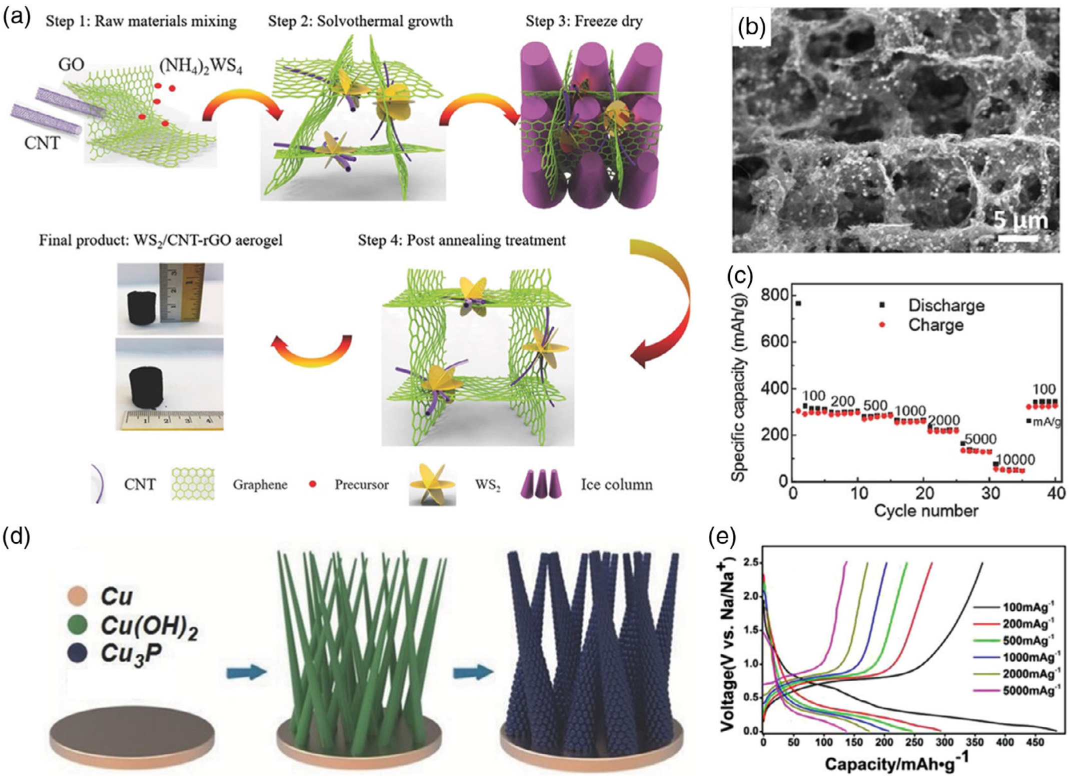

Figure 5. Conversion-type materials in Na ions storage. a) Schematic diagram for the preparation process of 3D WS_2/CNT-rGO aerogel. b) SEM image of WS_2/CNT-rGO-200 aerogel. c) Rate capability of WS_2/CNT-rGO-200 measured from 100 to 10 000 mA g^{-1}. Reproduced with permission.[93] Copyright 2016, Wiley-VCH. d) Schematic illustration of the preparation process of CPNWs. e) The GCD profiles of CPNW obtained from 100 to 5000 mA g^{-1}. Reproduced with permission.[96] Copyright 2016, Wiley-VCH.

treatment.[106] The 1D carbon channels not only boosted the ionic and electronic transport, but also confined the volume expansion of RP. Moreover, 3D frameworks interconnected by 1D nanofibers promoted the surface contact between electrolyte and electrode, increasing the electrochemical activity of microelectrode hybrid. Consequently, the freestanding RP@PMCNFs showed excellent cycle stability with 700 mAh g^{-1} at 2 A g^{-1} even after 920 cycles, demonstrating highly reversible alloying reaction. Based on the understanding of Fick's law, diffusion time can be assessed by $\tau \propto \frac{L^2}{D}$, where L is the diffusion length and D represents the diffusion coefficient of ions. Clearly, the diffusion kinetics can be extremely accelerated by reducing the diffusion distance in view of the square relationship in the equation. Thereby, nanostructured alloy materials with large surface area can efficiently shorten diffusion length, significantly improving the ions transport kinetics (**Figure 6**). Importantly, nanostructuring plays a significant role in decreasing pulverization and crack propagation behavior of electrodes during alloying/dealloying process by increasing surface energy and surface tension. The resultant counteracting stress effectively deals with the volume expansion.[45] The feasible strategy has been achieved by confining alloying nanodots in or distributing allying nanoparticle (NP) on conductive carbon matrix. For instance, Chen et al. prepared Sn nanodots with the size of 1–2 nm confined in porous N-doped carbon nanofibers (Sn NDs@PNC) (Figure 6a),[107] and Guo et al. distributed RP NPs (10–20 nm) in the 3D graphene aerogel coated with carbon layer (C@P/GA) by vapor phase deposition of PPy (Figure 6c,d).[108] The well-developed porosity and high electrical conductivity of carbon matrix not only promoted the transport of Na ions and electrons, but also improved the wettability of hybrid electrodes. As a consequence, the as-prepared Sn NDs@PNC and C@P/GA displayed considerable first charge capacity 631.2 mAh g^{-1} with ICE of 70% and fantastic capacity of 1095.5 mAh g^{-1} with high CE of 93.3% at 1 C even after 200 cycles (Figure 6b,e), respectively. It is noted that, after being subjected to long-term continuous charge/discharge test, the Sn NDs@PNC and C@P/GA electrodes still maintained their initial integrity of structure and morphology (Figure 6b,f), suggesting that the optimized nanostructure successfully prevented pulverization from volume expansion. Although these results suggest the merits of nanostructures for alloy anodes in Na ion storage, highly reactive surface of nanoalloying materials may result in undesirable electrochemical behavior, e.g., unstable SEI film, and incomplete alloying reaction. Clearly, nanostructuring is not a universal solution for alloying anodes, and other strategies should be used in conjunction by understanding the fundamentals of microelectrodes.

Inevitably, the ionic diffusion coefficient also plays a significant role in diffusion kinetics. The diffusion coefficient is exponentially related to the active energy according to Arrhenius equation, $D = A\exp\left(-\frac{\Delta G}{k_B T}\right)$, where A denotes the preexponential factor, ΔG represents the diffusion energy barrier, k_B denotes the

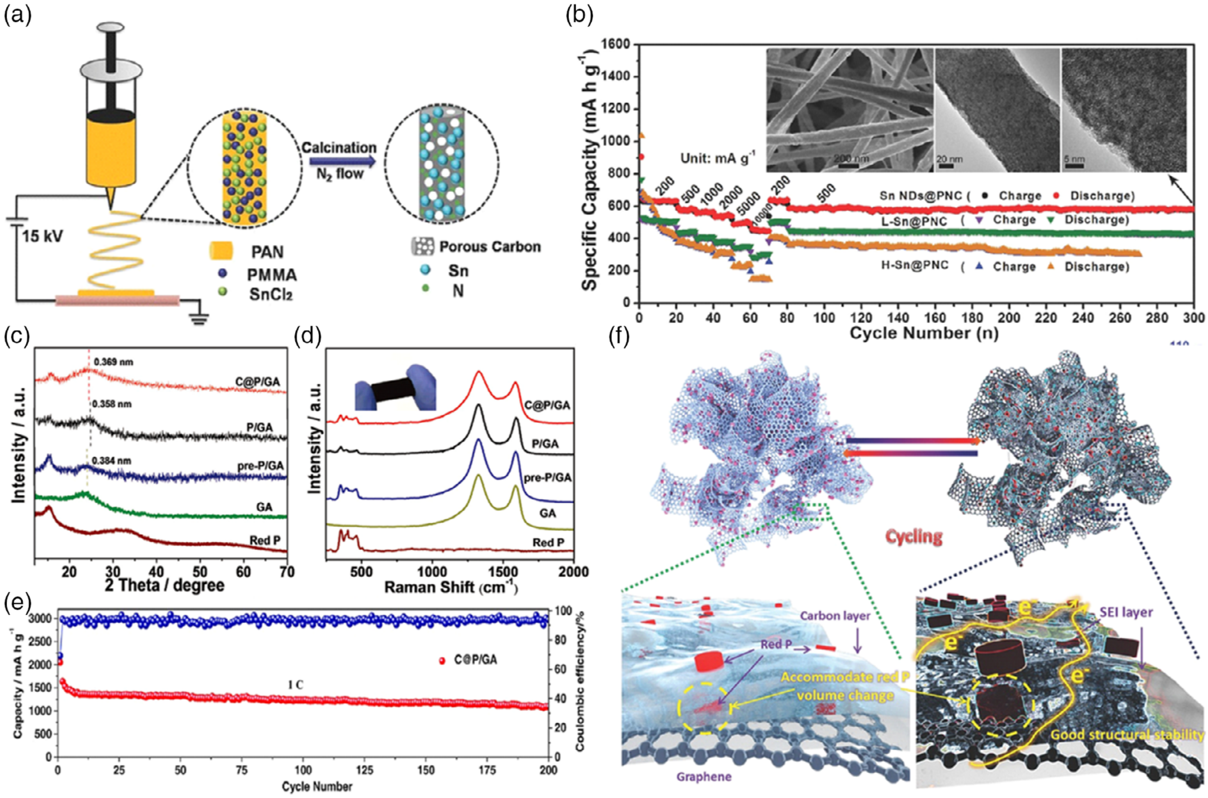

Figure 6. Alloying-type materials in Na ions storage. a) Schematic illustration of the preparation process for Sn NDs@PNC nanofibers. b) Rate and cycling performance of Sn NDs@PNC. Insets are the SEM, transmission electron microscopy (TEM), and high-resolution TEM images of Sn NDs@PNC after 300 cycles. Reproduced with permission.[107] Copyright 2015, Wiley-VCH. c) XRD patterns and d) Raman spectra of precursors and C@P/GA composites. The inset is a digital photograph of the as-prepared C@P/GA composite. e) Cycling stability of C@P/GA hybrid at the current density of 1 C. f) Schematic showing the evolution of C@P/GA as anode for NIB. Reproduced with permission.[108] Copyright 2016, Wiley-VCH.

Boltzmann constant, and T denotes the temperature. It will be an effective approach to enlarge interlayer spacing of electrode materials to mitigate energy barrier and thereby boost diffusion coefficient. For example, in 2D few-layer antimonene (FLA) with anisotropic alloying/dealloying process, it is easier for Na ions to traverse along the a/b-axis with a trivial diffusion energy barrier of 0.14 eV, delivering outstanding capacity of 642 mAh g^{-1} at 0.1 C.[109] Furthermore, the excellent cycle capability with capacity of 620 mA g^{-1} at 0.5 C after 150 cycles indicated Sb atoms with high utilization ratio of 93.9%. However, the anisotropic reaction process of FLA led to the undesirable volume expansion in specific direction. Therefore, amorphous materials without crystal orientation can eliminate the anisotropic volume expansion to a large extent, excellently restraining the pulverization of electrodes in continuous alloying reaction. For instance, Deng et al. prepared the amorphous intermetallic alloy phase Co–Sn for Na ion storage, in which Sn with electrochemical activity performed high capacity in Na ion storage and inactive Co functioned as a conductive inactive scaffold.[110] The optimized amorphous alloying electrode showed superior rate capability in comparison with low-crystalline and crystalline alloy phase. The aforementioned achievements prove that structure modulation, morphology regulation, and composite hybrid strategies can effectively tackle the awful volume expansion and deficient reversibility of alloying materials.

In the three reaction mechanisms discussed earlier, it is clear that the electrochemical performance of the respective microelectrodes can be enhanced by mediating the intrinsic properties of materials, such as the electrical conductivity of intercalation materials and the volume expansion, structure integrity of conversion/alloying materials, contributing to high performance of microdevices.[111–114]

4. Sodium Ion Micro-electrochemical Energy Storage Devices

Owing to the stable microelectrodes with well-designed structure, NIMEESDs have emerged and gradually been adapted to multiple functions such as flexibility and stretchability. The development milestones and recent evolution of NIMEESDs are briefly shown in **Figure 7**. The all-solid-state film battery was initially developed by Hayashi and co-workers, consisting of TiS_2 cathode, Na–Sn alloy anode, and Na_3PS_4 glass-ceramic solid electrolyte with high ionic conductivity.[115] Soon after, 2D stacked NIMCs and NIMBs were reported and then flexible belt- and fiber-shaped aqueous

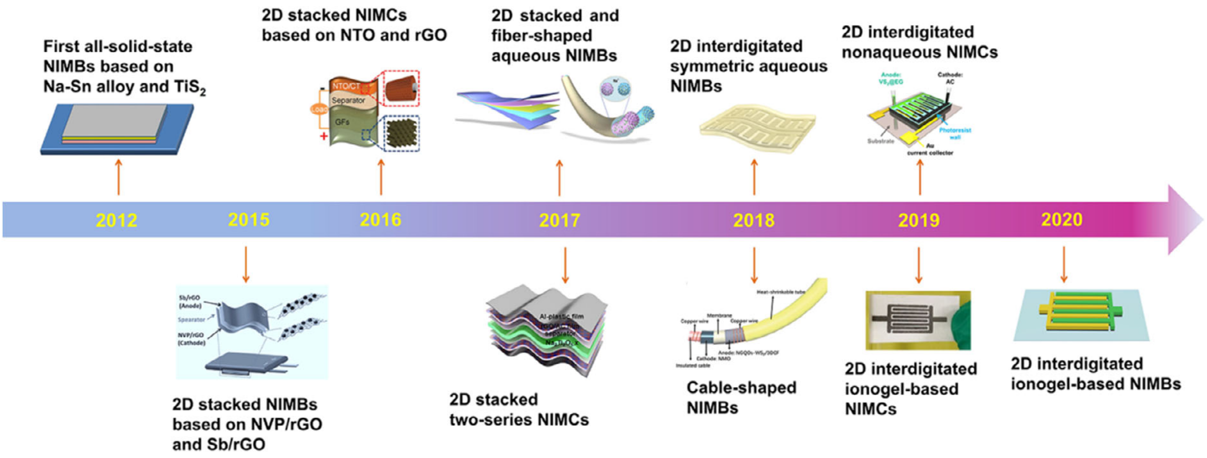

Figure 7. The timeline of the development of various NIMEESDs. Inset images: "2D stacked NIMBs based on NVP/rGO and Sb/rGO." Reproduced with permission.[116] Copyright 2018, Wiley-VCH. "2D stacked NIMCs based on NTO and rGO." Reproduced with permission.[117] Copyright 2016, Wiley-VCH. "2D stacked and fiber-shaped aqueous NIMBs." Reproduced with permission.[118] Copyright 2017, Elsevier. "2D stacked two-series NIMCs." Reproduced with permission.[121] Copyright 2017, American Chemical Society. "2D interdigitated symmetric aqueous NIMBs." Reproduced with permission.[120] Copyright 2018, American Chemical Society. "Cable-shaped NIMBs." Reproduced with permission.[127] Copyright 2018, Royal Society of Chemistry. "2D interdigitated nonaqueous NIMCs." Reproduced with permission.[129] Copyright 2019, Wiley-VCH. "2D interdigitated ionogel-based NIMCs."[40] "2D interdigitated ionogel-based NIMBs." Reproduced with permission.[30] Copyright 2020, Royal Society of Chemistry.

NIMBs were designed.[116–118] Since 2018, the 2D interdigitated plane NIMBs and NIMCs has experienced a "research boom" and extended to aqueous, nonaqueous, and ionogel-based electrolytes. The critical electrochemical performances of NIMBs and NIMCs are shown in **Table 3**.

4.1. 2D Stacked NIMEESDs

2D stacked NIMBs with sandwich configuration were first reported using solid-state electrolyte.[115] Remarkably, the binder-free conversion-type CPNW microelectrode has already shown superior rate and cycle capability as anode (Figure 4e). The pouch-type full cell fabricated with NVP cathode and CPNWs anode exhibited high capacity of 209 mAh g^{-1} based on the mass of CPNMs at 600 mA g^{-1} operated in the solvents of ethylene carbonate (EC) and dimethyl carbonate (DMC), and provided energy density of 104.5 Wh kg^{-1}.[96] Furthermore, the as-assembled NIMB could light a flexible light-emitting diode (LED) screen, hinting at possible application in future wearable microelectronics. However, the nonnegligible volume expansion of CPNWs hindered the long cyclability of NIMBs with a deteriorative capacity of 79.9 mAh g^{-1} after 200 cycles. This seems to be a recurring problem for conversion-type electrodes, reaffirmed by poor cycling of CuO arrays anode paired with $Na_{0.67}(Ni_{0.23}Mg_{0.1}Mn_{0.67})O_2$ cathode which was stable for only 40 cycles.[84] Lu et al. boosted the Na ion storage of TiO_2 through surface engineering, in which the TiO_2 nanotube arrays were phosphorylated by NaH_2PO_2 (P-TiO_2).[119] The optimized P-TiO_2 showed near-zero strain with the negligible change of characteristic diffraction peaks and distortion of lattice spacing during intercalation/deintercalation process, and high surface reactivity with accelerated Na ions insertion behavior.[43,45] Impressively, the NIMBs consisting of P-TiO_2 anode and carbon-coated NVP (NVP/C) cathode delivered excellent capacity of 111 mAh g^{-1} with high voltage plateau at 3.4 V, and outstanding energy density of 150 Wh kg^{-1} on the basis of both anode and cathode. Unfortunately, the reported microdevices relied on toxic organic solvents that are intolerable in wearable devices.[16,21,113] To address this issue, a feasible route is to develop moderate electrolytes for NIMEESDs. For instance, Wang et al. fabricated flexible and belt-shaped NIMBs composed of $Na_{0.44}MnO_2$ (NMO) cathode, carbon-coated $NaTi_2(PO_4)_3$ (NTPO@C) anode, and polyacrylonitrile (PAN) separator soaked by 1 M Na_2SO_4 electrolyte.[118] The as-fabricated NMO//NTPO@C NIMBs showed specific capacity of 43 mAh g^{-1} at 0.1 A g^{-1} and excellent rate capability with 27 mAh g^{-1} at 5 A g^{-1} measured in the voltage of 0–1.6 V. Impressively, the NIMBs delivered high volumetric energy density of 23.8 mWh cm^{-3}. It was noted that the packaged sandwich-shaped NIMBs exhibited satisfactory mechanical flexibility under different bending angles and continuous bending testes. In addition, Deng et al. fabricated a symmetric NIMB based on $Na_2VTi(PO_4)_3$ (NVTP) electrodes embedded in carbon sphere and biocompatible electrolyte, including NaCl, normal saline, and simulated body fluid (SBF).[120] This symmetric NIMB encapsulated by silk fibroin presents the perfect platform to demonstrate a safe, biocompatible, and cheap alternative to conventional implantable medical devices. Furthermore, the high energy density coupled with efficient rate capability provided windows for a wide range of in vivo applications.

In contrast to NIMBs, NIMCs usually consist of high-capacity battery-type anode and high power electric double-layer capacitors (EDLCs)-type cathode, working under a Daniell-type mechanism with Na ion being inserted/extracted into/from the anode and anion adsorption/desorption at the cathode surface.[20] The key challenge for NIMCs lies in the proper trade-off between slow anode and fast cathode, exhibiting typical battery- or capacitor-type kinetics. This was achieved in a flexible NIMC assembled with NTO nanosheet arrays growth on reduced

Table 3. Summary of electrochemical performance of various configuration NIMEESDs. V, voltage; C, specific capacity or capacitance.

Types	Electrodes	Electrolyte	V	C	Energy density	Power density	Stability	Flexibility	Ref.
2D stacked NIMBs	CPNWs//NVP	1 M $NaClO_4$/EC/DMC/FEC	2.0–4.0	209 mAh g$^{-1a)}$	104.5 Wh kg$^{-1b)}$	–	–	–	[96]
	P-TiO_2//NVP/C	1 M $NaClO_4$/EC/DMC/FEC	2.3–4.9	107 mAh g$^{-1c)}$	150 Wh kg$^{-1b)}$	–	–	–	[119]
	NTPO@C//NMO	1 M Na_2SO_4	0–1.6	43 mAh g$^{-1c)}$	23.8 mWh cm$^{-3d)}$	3.8 W cm$^{-3d)}$	1000 (62%)	180° 100 times	[118]
	NVTP//NVTP	SBF	0–1.5	52.9 mAh g$^{-1b)}$	–	–	800 (74%)	–	[120]
2D stacked NIMCs	GF//NTO/CT	1 M $NaClO_4$/EC/DEC	1.0–3.0	–	0.2 mWh cm$^{-2b)}$	10.5 mW cm$^{-2b)}$	2500 (80.3%)	–	[117]
	rGO/AC//$Na_2Ti_2O_{5-x}$//rGO/AC	1 M $NaClO_4$/EC/DMC	1.0–3.8	–	15.6 mWh cm$^{-3d)}$	120 mW cm$^{-3d)}$	5000 (82.5%)	Bendable	[121]
	NVOPF//VO_2	1 M $NaClO_4$/EC/PC/FEC	1.0–4.0	90 mAh g$^{-1b)}$	215 Wh kg$^{-1b)}$	5200 W kg$^{-1b)}$	220 (80%)	Bendable	[123]
Fiber-shaped NIMBs	NTPO@C//NMO	1 M Na_2SO_4	0–1.6	46 mAh g$^{-1c)}$	25.7 mWh cm$^{-3b)}$	0.7 W cm$^{-3b)}$	100 (76%)	180° 100 times	[118]
	Na//NiS_2⊂PCF	1 M $NaClO_4$/EC/PC/FEC	0.01–3.0	679 mAh g$^{-1c)}$	–	–	5000 (76%)	150° (89%)	[126]
	NGQDs-WS_2//NMO	1 M $NaPF_6$/EC/DEC/FEC	1.5–3.6	0.186 mAh cm$^{-1e)}$	–	–	–	–	[127]
	Na//PB@GO@NTC	1 M $NaPF_6$/EC/DMC	2.0–3.8	87 mAh g$^{-1c)}$	256 Wh kg$^{-1d)}$	–	120 (76%)	180°	[125]
2D in-plane NIMCs	AC//VS_2@EG	1 M $NaClO_4$/EC/DEC/FEC	0.01–3.5	110.7mF cm$^{-2b)}$	188.3 μWh cm$^{-2b)}$	0.35 mW cm$^{-2b)}$	5000 (≈100%)	–	[129]
	NTO//AG	NaTFSI/P_{14}TFSI/PVDF-HFP	0–3.5	19.5 F cm$^{-3b)}$	37.1 mWh cm$^{-3b)}$	1.2 W cm$^{-3b)}$	6000 (75%)	180° (100%) 2000 times	[40]
2D in-plane NIMBs	NTO//NVP	$NaBF_4$/$EMIMBF_4$/PVDF-HFP	0.8–2.8	30.7 mAh cm$^{-3d)}$	55.6 mWh cm$^{-3d)}$	1.5 W cm$^{-3d)}$	3000 (70%)	180° (100%) 1000 times	[30]
	NTO//NVP	NaTFSI/EMIMTFSI/PVDF-HFP	0.8–2.8	15.1 mAh cm$^{-3d)}$	32.6 mWh cm$^{-3d)}$	–	–	–	[30]

a)Reported values based on anode mass; b)Reported values on the basis of electrode area, volume or mass; c)Reported values based on cathode mass; d)Reported values according to volume of device; e)Calculated values based on the reported literatures.

graphene oxide film (GFs) and carbon textiles (NTO/CT) as cathode and anode, respectively.[117] 3D array network accelerated charge transport and the ultrathin NTO nanosheets dramatically shortened the pathways for electrolyte ion diffusion in the electrode. Consequently, the as-fabricated GF//NTO/CT showed excellent capacitance retention of more than 80.3% after 2500 cycles at $0.5\ A\ g^{-1}$, and maximum power density of $70\ mW\ cm^{-3}$ and volumetric energy density of $1.3\ mWh\ cm^{-3}$ based on the volume of device. Moreover, the NIMCs showed prominent mechanical flexibility with capacitance retention of 100% under different bending states. Apart from utilizing a conductive matrix to increase conductivity of NTO, it is an effective strategy to improve intrinsic conductivity by introducing oxygen vacancies. For example, the $Na_2Ti_2O_{5-x}$ nanowire arrays showed enhanced rate capability with $72\ mAh\ g^{-1}$ even at 50 C, 8 times higher than pure NTO electrode, attributed to the narrow bandgap and structural stability of $Na_2Ti_2O_{5-x}$ arrays with oxygen vacancies.[121] Remarkably, the two serially connected NIMCs based on rGO/AC cathode and $Na_2Ti_2O_{5-x}$ anode on Ti foil with two sides displayed volumetric power density and energy density of 120 and $15.6\ Wh\ L^{-1}$, respectively, and reliable cycling life with 82.5% capacitance retention after 5000 cycles. The flexible rGO/AC//$Na_2Ti_2O_{5-x}$//rGO/AC NIMCs could power 40 LEDs simultaneously for 15 min in both relaxed and bent states, demonstrative of the promising application in microelectronics. Despite this demonstration, 2D stacked NIMCs and NIMBs still use conventional metal (e.g., Cu, Ti) current collectors as substrate. These have limited range of flexibility and cannot be adapted to flexible microelectronics, urging us to look for modern alternatives.[84,121,122]

Different from the Daniell-type mechanism in NIMCs, the rocking-chair mechanisms based on battery-type cathode and capacitive-type anode allow Na ions adsorption on anode surface and extraction from cathode during charge process.[20] To boost the kinetics matching between intercalation-type cathode and high-rate anode, a 3D-oriented $Na_3(VO)_2(PO_4)_2F$ (NVOPF) array evolved from VO_2 array on graphene foam scaffold was prepared through solvothermal method (**Figure** 8b,d).[123] The binder-free NVOPF arrays and NVOPF slurry electrode showed the same capacity of $130\ mAh\ g^{-1}$ at 0.5 C, whereas the arrays showed

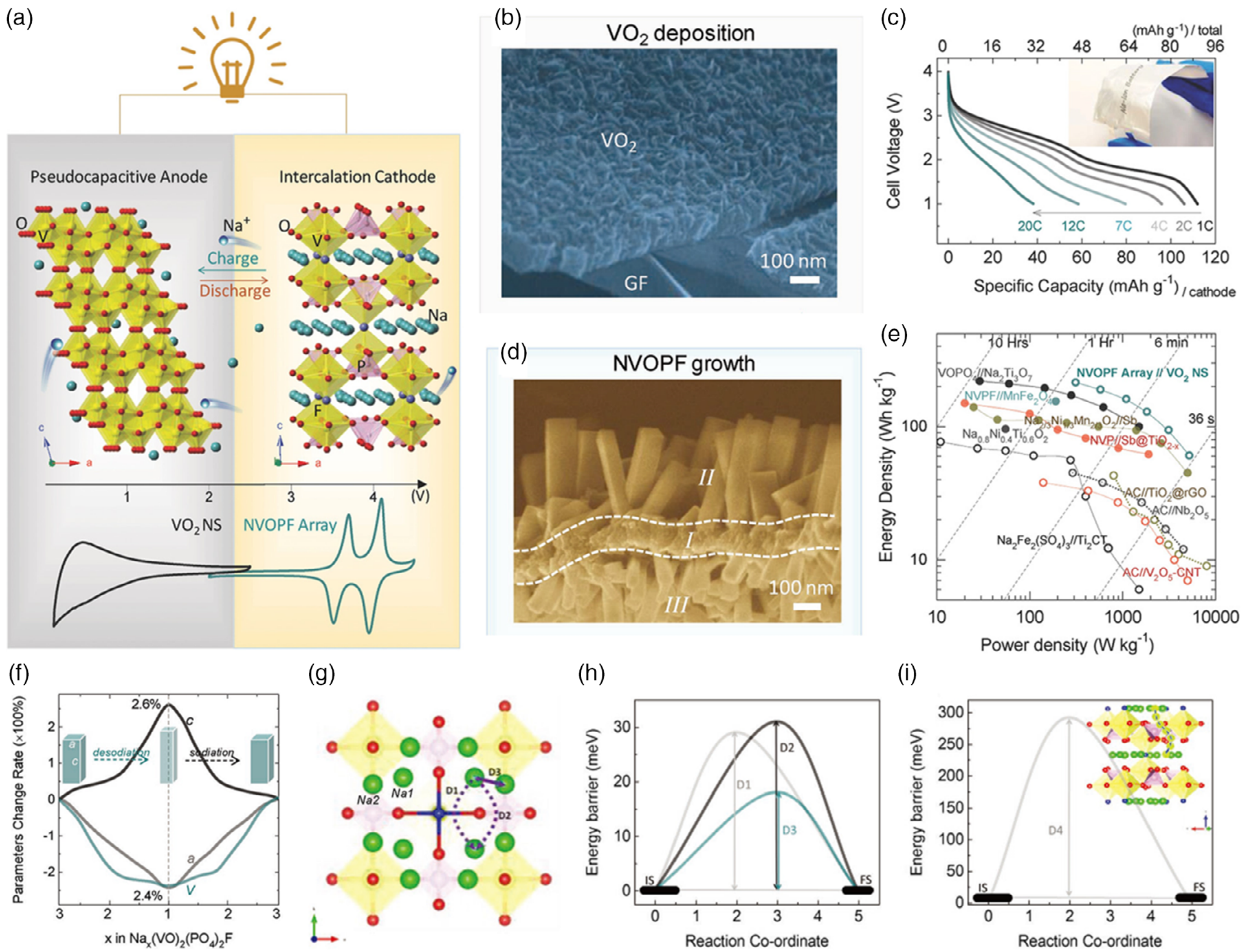

Figure 8. 2D stacked NIMCs. a) Schematic illustration of NVOPF//VO_2 NIMC. b) SEM image of the GF-VO_2 nanosheet. c) GCD profiles of NVOPF//VO_2 NIMC from 1 to 20 C (1 C = 130 mA g^{-1}). Inset is the digital image of soft-packed pouch cell. d) SEM image of GF-NVOPF array electrode. e) Ragone plot of NVOPF//VO_2 NIMC compared with other reported devices. f) Changes of lattice parameters in *a*, *c*, and volume during Na ion extraction/insertion. g) First-principle calculation of diffusion pathways in plane (*ab*). h) The energy barriers for Na ion diffusion in plane (*ab*). i) First-principles calculation of Na ion migration barrier in *c*-direction. Reproduced with permission.[123] Copyright 2018, Wiley-VCH.

superior rate capability with considerable capacity of 42 mAh g^{-1} at 60 C in comparison with the destructive slurry electrodes with negligible capacity of 7 mAh g^{-1}, as well as the distinguished cycle performance with 90% retained after 10 000 cycles with tiny volume change of only 2.6% after desodiation process (Figure 8f), demonstrating that the NVOPF arrays can engage the long-life and high-power microdevices with fast charge/discharge. The as-fabricated soft-packed NIMCs based on NVOPF cathode with Na ions deintercalation and VO_2 anode with Faradic reaction at the interface revealed a reversible capacity of 90 mAh g^{-1} at 1 C, and still retained 40 mAh g^{-1} at 20 C assessed from only cathode mass in the voltage range of 1–4 V (Figure 8a,c), which was helpful to implement high-power microdevices. Consequently, the all-vanadium-based NVPOF//VO_2 NIMCs delivered remarkable power density 5200 W kg^{-1} (Figure 8e). The obtained NIMCs with the outstanding performance cannot be separated from (002) orientation NVOPF arrays, in which the low energy barrier of Na ions' in-plane migration makes for fast Na ion diffusion (Figure 8h,i). It is a promising way to design an optimized structure with enhanced Na ions migration for high-power NIMCs, meanwhile forming the strong structure–function relationship between microelectrode structure and device performance.

4.2. Fiber-Shaped NIMBs

The advent of 1D fiber-shaped NIMBs (e.g., parallel, coaxial, and twisted types) marked a revolution in wearable integrated power supply due to a myriad of features such as miniaturization, adaptability to different mechanical states, and substrate-free compatibility with textile.[51,124] Generally, flexible fiber-type NIMBs exhibit excellent mechanical flexibility under different states (e.g., bending, twisting). In particular, the fabric woven by fiber-shaped NIMBs exhibited good air permeability and flexibility, which is necessary for wearable microelectronics. For instance, Yan and co-workers made the best of waste laboratory coat and Ni ions from industrial wastewater to construct Ni-coated cotton textile (NCT) through electroless nickel plating as a flexible current collector, which exhibited good conductivity and wettability.[125] Subsequently, Prussian blue and graphene composites were prepared on NCT (PB@GO@NCT), showing capacity of 101 mAh g^{-1} at 1 C and outstanding cycle capability with capacity retention of 84.4 % at 5 C after 1800 cycles by synergistic effect between high-capacity PB and conductive NCT. Further in the same direction, the tube-shaped NIMBs consisting of PB@GO@NCT cathode, metal sodium foil, and hollow Teflon tube were realized, which could power a LED under flat and foldable states, and delivered a considerable cycle life with capacity retention of 76% after 120 cycles and maximum energy density of 260 Wh kg^{-1} (**Figure 9**a–f). This is a proof that the intercalation-type materials with robust structure not only work in sandwich configuration microdevices, but are also suitable for fiber-shaped structure. Transition metal dichalcogenides (TMDs) have shown promising results in this field by virtue of their metallic nature with fast diffusion kinetics and weak Van der Waals force in lamellated structure. For example, the yolk-shell NiS_2 NPs embedded in porous carbon fiber (NiS_2@PCF) composites provided high surface area and excellent electrode integrity without pulverization and crack, displaying superior rate capacity and satisfactory cycle lifespan. The as-assembled NIMBs on the basis of NiS_2@PCF showed excellent mechanical flexibility, which powered a LED under various bending angles and multiple bending times (Figure 9g).[126] WS_2 with a larger interlayer spacing of 0.62 nm than graphite and small volume expansion enables intercalation of Na ions. 3D carbon foam provided a suitable substrate for growing WS_2 nanosheets decorated on nitrogen-doped graphene quantum dots (NGQDs), which were grown on 3D carbon foam matrix as the anode of NIBs.[127] Nanostructured NGQDs enhanced the capacitive contribution to the hybrid electrode benefitting from the high specific surface area, in which the enhanced hybrid electrode delivered exceptional cycle life with retention of 97.1% after 1000 cycles and superior rate capability with 125.1 mAh g^{-1} at 5000 mA g^{-1}. Using the same material as anode, cable-shaped NIMBs with

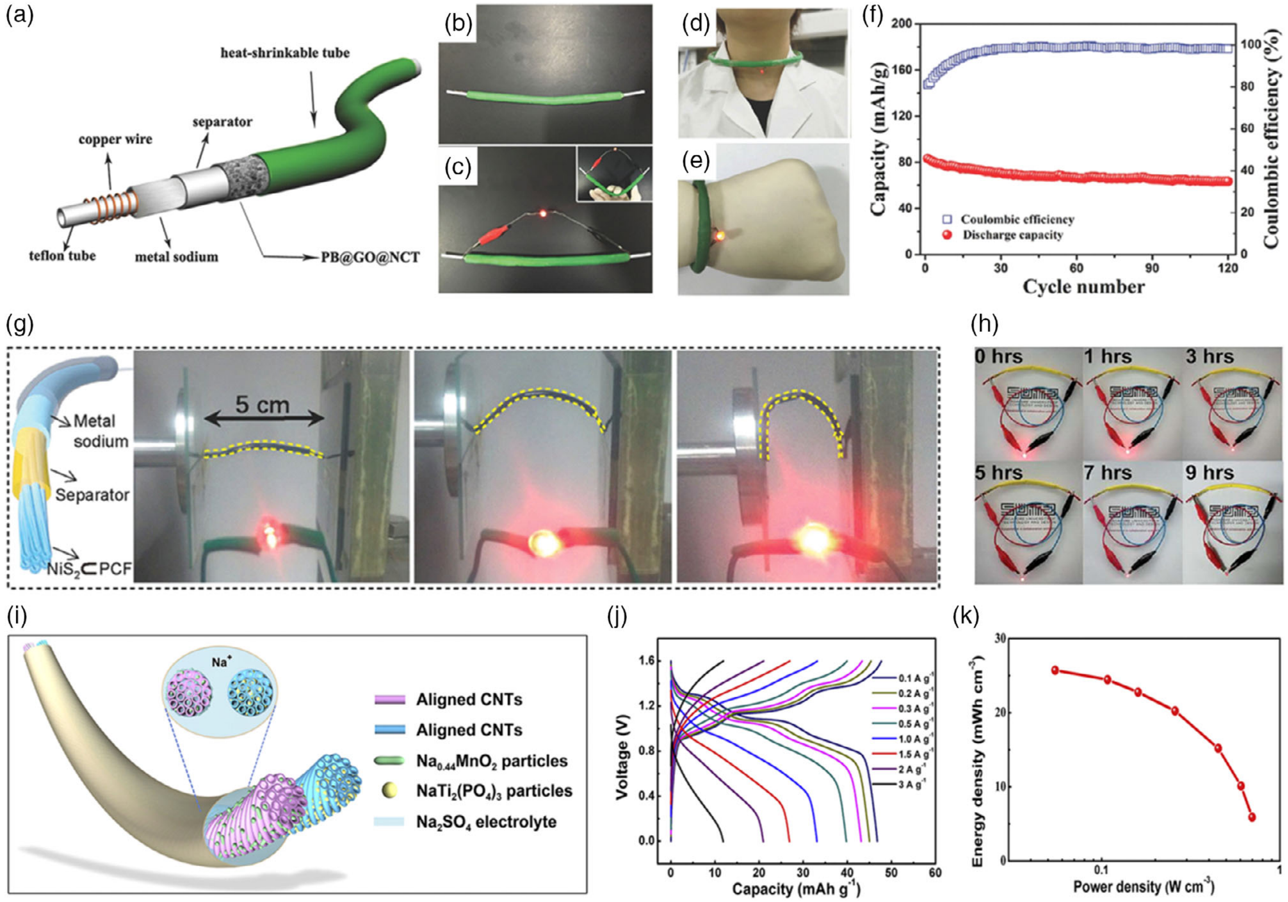

Figure 9. Fiber-shaped NIMBs. a) Schematic showing the configuration of the tube-type NIBs. b) Digital image of the NIBs. c–e) Digital images of a LED powered by tube-type NIBs under different bending states. f) Cycles performance of tube-type NIBs at 100 mA g^{-1}. Reproduced with permission.[125] Copyright 2017, Wiley-VCH. g) Schematic illustration of the fiber-shaped NIB and digital images of LEDs powered by the fabricated fiber-shaped NIB under different bending states. Reproduced with permission.[126] Copyright 2018, Wiley-VCH. h) A LED powered by a 7 cm cable-shaped NIB for 9 h. Reproduced with permission.[127] Copyright 2018, Royal Society of Chemistry. i) Schematic illustration of the configuration of fiber-shaped NIB. j) GCD profiles of fiber-shaped aqueous NIB at various current densities. k) Ragone plot of fiber-shaped aqueous NIB. Reproduced with permission.[118] Copyright 2018, Elsevier.

$Na_{0.44}MnO_2$/Ni-foam cathode showed considerable capacity of 59.8 mAh g^{-1} at 50 mA g^{-1} (the mass of anode and cathode), and could light a LED for 9 h (Figure 9h). Therefore, the intercalation-type and TMDs materials are both beneficial to construct the fiber-shaped NIMBs with excellent flexibility.

While considering wearable MEESDs, organic electrolytes in liquid state are particularly unsuitable for such fiber-shaped devices upon integration with wearable and implanted medical application. This is partly due to their intrinsic flammability and possible toxicity, both of which when added to the risk of leakage pose a serious threat to personal health and safety. To tackle this issue, Wang et al. designed fiber-shaped NIMBs based on CNT/NMO cathode and CNT/NTPO@C anode that took advantage of high tensile strength and conductivity of 1D CNT fiber, working with Na ion-based aqueous electrolyte (Figure 9i).[118] The as-fabricated fiber-shaped NIMBs were operated in 1.0 M Na_2SO_4 aqueous electrolyte, in which it showed considerable energy density of 25.7 mWh cm^{-3} (Figure 9j,k). The fiber-shaped NIMBs can maintain the charge–discharge characteristics in saline that is compatible with living body, significantly advancing safe aqueous fiber-shaped NIMBs for wearable microelectronics. Overall, these fiber-shaped NIMBs show unique lateral dimension with long diffusion length, thus the deteriorated electrochemical performance restricted the current fiber-type NIMBs at centimeter scale.

4.3. 2D In-Plane NIMEESDs

The typical 2D in-plane NIMEESDs are composed of current collector, interdigital microelectrodes, and electrolytes on the same substrate, constructed by photolithography or other mask-assisted processes.[128] Interestingly, the separator of in-plane NIMEESDs is different from conventional separator, which present tiny interspace between interdigitated fingers, greatly decreasing the barrier to Na ions migration, realizing high-power NIMEESDs. As discussed before, battery-type anodes have sluggish kinetics compared with EDLC-type cathode based on adsorption/desorption surface process, which weakens the kinetic balance between rate capability and power density of NIMCs. Therefore, conductive networks of anodes should be paid attention to match with the high-rate cathodes. As a demonstration, vertically aligned VS_2 nanosheets were anchored on electrochemically exfoliated graphene (VS_2@EG) through solvothermal method and postthermal treatment process (**Figure 10**c).[129] The as-prepared VS_2@EG as anode for Na ions storage exhibited impressive surface-controlled contribution of more than 79%, suggesting that the sufficient open spaces between adjacent VS_2@EG nanosheets shortened the diffusion pathways of Na ions and facilitated the penetration of electrolyte into available active sites. Consequently, the interdigital NIMCs were fabricated based on VS_2@EG anode and AC cathode slurry, which were injected into the prepatterned microchannels on gold current collector. The as-fabricated NIMCs were operated at $NaClO_4$ electrolyte with Na ions insertion into VS_2@EG and ClO_4^- ions adsorption on AC surface (Figure 10a,b). The AC/VS_2@EG NIMCs delivered extraordinary cycle life without capacitance fade at 1 mA cm^{-2} in the voltage of 0–3.5 V. However, the binder in the slurry restricted high real energy and power density of NIMCs. To overcome the problem, our group proposed a simple mask-assisted filtration strategy to construct metal-free current collector planar NIMCs based on activated graphene (AG) cathode with abundant nanopores and urchin-like NTO anode, where the EG nanosheets were used as flexible current collector and conductive additives in sluggish kinetics of anode (Figure 10e).[40] The NTO//AG NIMCs with fast charge and kinetics matching delivered an excellent capacitance of 19.5 F cm^{-3} with obvious hybrid ions capacitive behavior in bis(trifluoromethanesulfonyl)imide sodium salt (NaTFSI)-based ionogel electrolyte, where the Na ions inserted/extracted into/from NTO and $TFSI^-$ ion desorbed/adsorbed at AG surface (Figure 10f). Furthermore, the NTO//AG NIMCs presented extraordinary self-discharge time of 44 h from 3.5 to 0.6 V and outstanding flexibility without capacitance fade under various bending angles that ensured the practicability in microelectronics (Figure 10g,h). It should be mentioned that the interdigital in-plane NIMCs possess multidirectional ions diffusion kinetics, in which electrolyte ions could not only transport between two side surfaces of microelectrodes, but also transport in the vertical direction of microelectrodes (Figure 10i,j), significantly enhancing the rate capability of NIMCs with the highest volumetric power density of 1200 mW cm^{-3}.

To broaden the application of NIMEESDs, our group also explored interdigital flexible NIMBs with $Ti_3C_2T_x$ MXene-derived NTO anode and NVP cathode by mask-assisted strategy on smooth nylon membrane, exhibiting excellent mechanical flexibility without delamination from substrate under twisted state (**Figure 11**a-c).[30] Interestingly, the interdigital planar NIMBs also showed multidirectional Na ions diffusion mechanism, indicative of its ubiquity in interdigital microdevices. It shows that the in-plane interdigital NIMEESDs enable high-power microdevices with fast charge process. The quasi-solid-state NIMBs were constructed with $NaBF_4$, 1-ethyl-3-methylimidazolium tetrafluoroborate ($EMIMBF_4$), and PVDF-HFP ionogel electrolyte ($NaBF_4$-IE). Remarkably, the NTO//NVP NIMBs delivered outstanding capacity of 30.7 mAh cm^{-3} at 1 C, and still retained up to 15.7 mAh cm^{-3} at 30 C (Figure 11d), as well as the exceptional long-term capability with tiny capacity loss of only 0.01% per cycle at 20 C for 3000 cycles. Such enhanced electrochemical performance of the as-fabricated NIMBs was attributed to higher ionic conductivity and Na ions transference number of $NaBF_4$-IE with nonflammability, and reversible intercalation/deintercalation process of NTO and NVP with robust structure (Figure 11e,f). In addition, NIMBs showed extraordinary high-temperature stability with capacity of 13.5 mAh cm^{-3} at 100 C under 100 °C, and exceptional power density of 4.0 W cm^{-3}, realizing fast charge–discharge response, which are promising candidates for microelectronics and integrated microsystem under harsh condition. Furthermore, the flexible NIMBs can output tailored voltage and current by fabricating self-integrated devices in series and parallel, respectively, in which three serially connected NIMBs could power the "DICP" patterns in severe bending states (Figure 11g). Such integration is even more fruitful in interdigital NIMBs with biocompatible electrolytes. A proof of concept was shown with the fabrication of symmetric NIMBs based on NVTP electrode as both cathode and anode embedded in carbon sphere interlaced by carbon fiber operated in normal saline and SBF electrolytes.[120] Three in-series connected interdigital NIMBs implanted in the body of rats could light a LED even after 1 month, demonstrating high reliability for implantable medical devices.

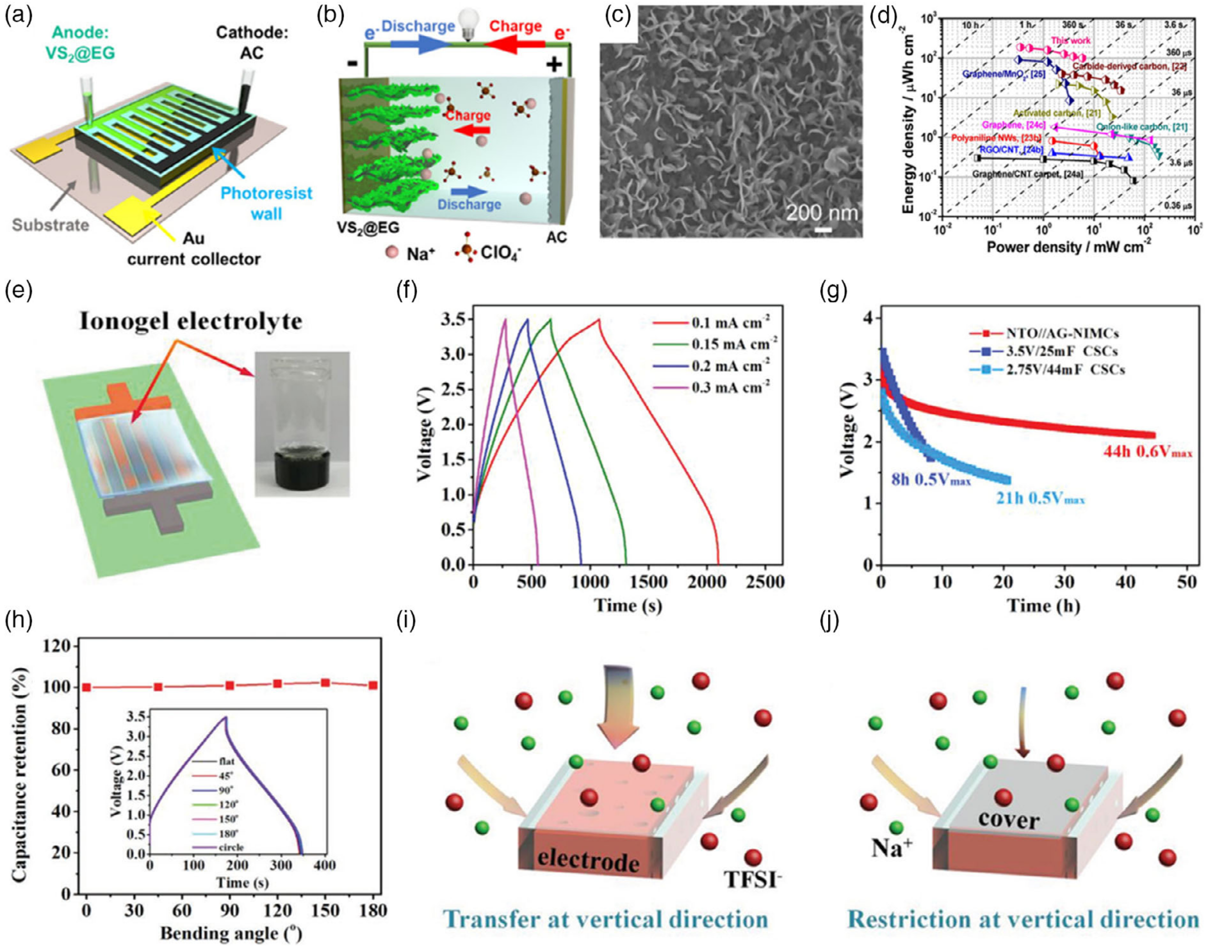

Figure 10. 2D in-plane NIMCs. a) Schematic showing the configuration of NIMC based on VS_2@EG anode and AC cathode. b) Reaction mechanism of VS_2@EG//AC NIMC. c) SEM image of VS_2@EG. d) Ragone plots of VS_2@EG//AC NIMC compared with to other reported MSCs. Reproduced with permission.[129] Copyright 2019, Wiley-VCH. e) Schematic of ionogel-based NTO//AG-NIMCs and the digital image of ionogel electrolyte on the basis of NaTFSI-P_{14}TFSI-PVDF-HFP. f) GCD profiles of NTO//AG NIMC tested from 0.1 to 0.3 mA cm^{-2}. g) Self-discharge curves of NTO//AG NIMC compared with commercial supercapacitors. h) Capacitance retention of NTO//AG NIMC under different bending angle. Inset is GCD profiles tested at various bending states. i) Schematic showing the multidirectional ion diffusion pathways at the interdigital microelectrodes without EG cover, and j) the restriction of ion transport at the vertical direction with EG cover. Reproduced with permission.[40] Copyright 2019, Wiley-VCH.

5. Summary and Perspectives

The implementation of on-chip NIMEESD is foreseen as a vital power supply solution for flexible microelectronics, smart bracelet, foldable screen, and wireless sensor systems. From 2D stacked-type, fiber-shaped to 2D in-plane NIMEESDs, the various microelectrodes have been intensively explored for the usage of high-performance NIMBs and NIMCs, especially the intercalation-type materials with robust structure and negligible volume expansion during sodiation/desodiation process. Despite great achievements of NIMBs and NIMCs, it should be noted that the improvement of energy and power densities for NIMEESDs with long-term stability and low self-discharge rate suitable for day-to-day microelectronics is still quite challenging to achieve. To realize high-performance NIMEESDs and practical application in microelectronics, the following challenges should be overcome, encompassing electrochemical active materials, device configuration, fabrication process, and multifunctional integration (**Figure 12**).

First, the electrochemical active materials are the footstone of high-performance NIMEESDs, including cathode, anode, and electrolyte materials. The impressive progress in battery-type electrode for NIBs has been made in the past 10 years, but there are still plenty of problems to be unsolved for NIMEESDs, for instance, the toxic components or precious transition metals in electrode materials,[130] the incompatibility between rigid electrode materials and flexible MEESDs,[131] and large volume expansion of anodes with conversion and alloying processes.[132] To address the aforementioned issues, it is effective to adjust the intrinsic electrode properties through valance adjustment, phase engineering, and surface modification to extract every bit of performance enhancement possible,[114,133] for instance, robust structure for periodic reversible sodiation/desodiation process and exceptional electrical conductivity for fast electrochemical

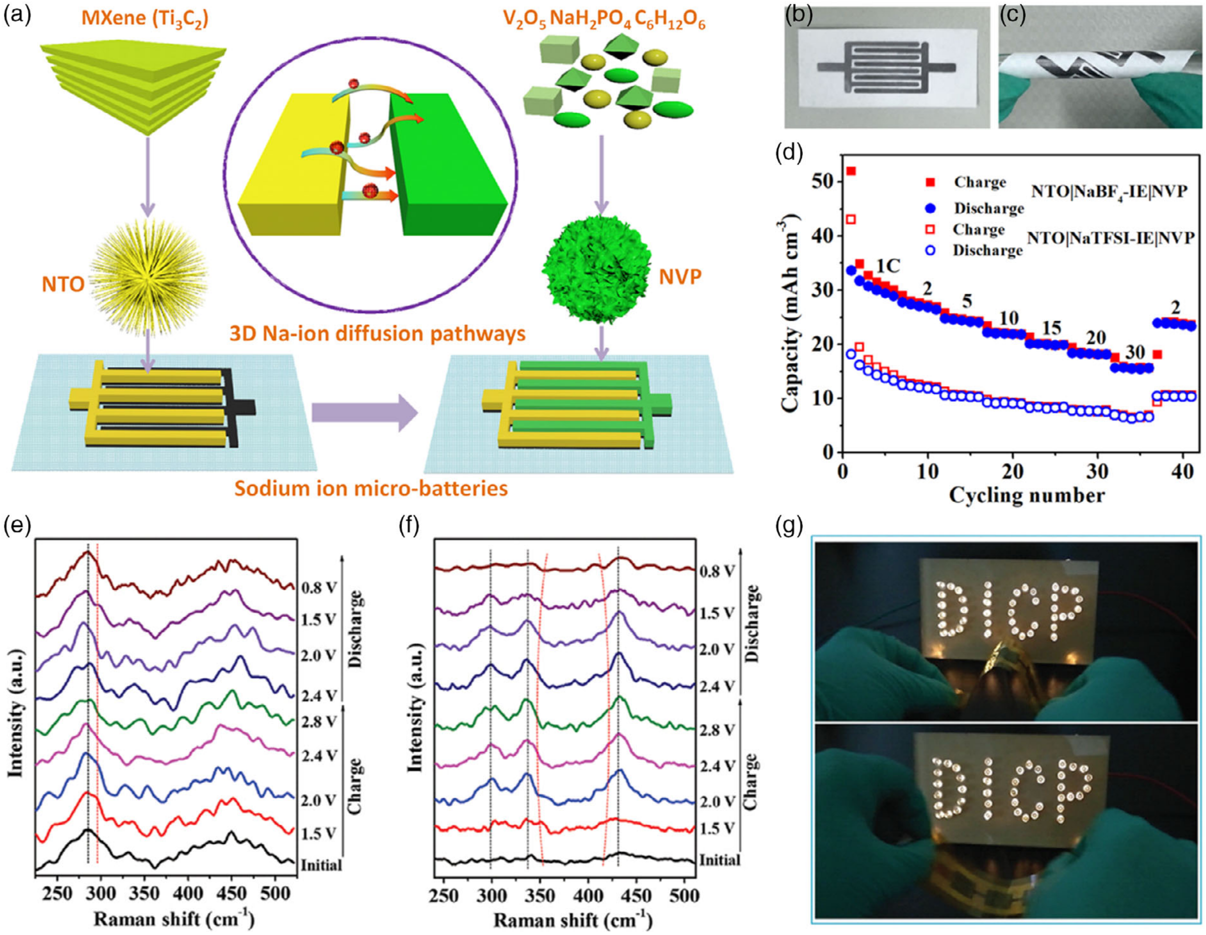

Figure 11. 2D in-plane NIMBs. a) Schematic illustration of the preparation process of NTO and NVP and fabrication of NIMB. Inset is the schematic illustration of 3D Na ion transfer during the discharge process. b,c) Digital images of NIMB in the flat (b) and twisted (c) states. d) Rate capability of NTO//NVP NIMBs. e,f) In situ Raman spectra of the e) NTO anode and f) NVP cathode during charge–discharge process. g) Digital images of the letters "DICP" composed of 42 LEDs powered by three tandem NTO//NVP under convex and concave states. Reproduced with permission.[30] Copyright 2020, Royal Society of Chemistry.

response. This is substantiated by nanohoneycomb SnS arrays with ultrathin nanosheets and smaller lateral sizes that deliver superior performance metrics compared with nanoflake and nanowall SnS arrays.[31] Besides the well-designed inorganic materials, organic materials (e.g., metal–organic frameworks, covalent organic frameworks) with porous structure may also provide novel opportunities for high-performance NIMEESDs in view of high capacity, fast diffusion kinetics, and structure stability.[134–136] Compared with high-capacity battery materials, it is also important to develop stable high-voltage cathode and low-voltage anode to work on high-energy NIMEESDs by rationally adjusting oxygen vacancies and heteroatoms doping. With regard to capacitive-type materials, carbon-based nanomaterials with high conductivity and excellent stability exhibit extraordinary electrochemical behavior in NIMCs. In particular, graphene showed non-Faradaic capacitance superior to conventional carbon materials, but the capacitance of EDLC-type materials based on the electrolyte ions adsorption/desorption on the surface of microelectrodes cannot match up to the pseudocapacitive material involving Faradaic reaction. For enhancing the capacitance contribution for NIMCs, forming in-plane nanopores not only increases the surface area of graphene, but also introduces abundant defects to accelerate the Na ions shuttle. In addition, it is a trustworthy strategy to introduce pseudocapacitive ingredients into graphene by surface functionalization or heteroatoms doping. In the development of high-performance electrode materials for NIMEESDs, the electrolytes should match with the as-prepared electrode materials (e.g., morphology, voltage window) to achieve high energy/power density. Importantly, the SEI layers on anode surface are strongly associated with electrolytes, which significantly affect the ICE. Inorganic solid-state electrolytes possess high voltage for NIMEESDs, but have the disadvantage of grain boundary resistance, inferior ionic conductivity, and poor mechanical flexibility, which mainly restrict their practicability for flexible NIMEESDs. Compared with inorganic solid-state electrolytes, liquid electrolytes with high ionic conductivity contribute to high-power NIMEESDs, but the fluidity of solvent could possibly cause electrolyte leakage. Differently, polymer gel electrolytes consisting of liquids hosted in polymer matrix are classified as aqueous, organic, and ionic liquid gel polymer

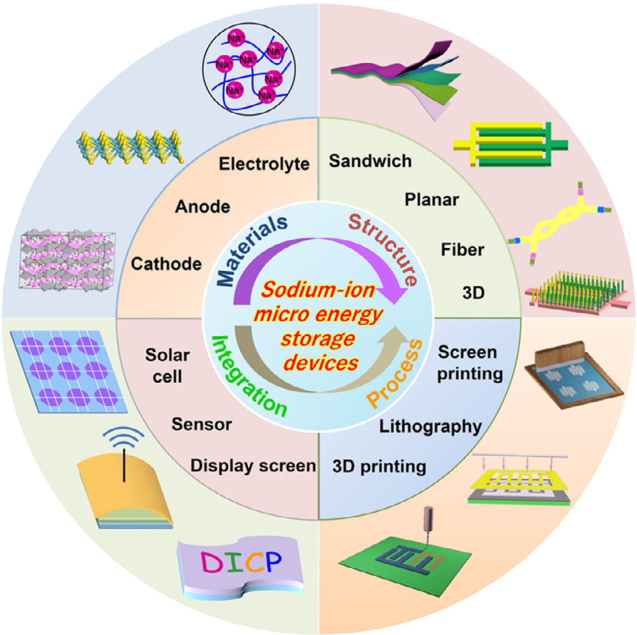

Figure 12. The research prospect of NIMEESDs from active materials, electrode structure, prepared approaches, and integrated system. Screen printing image. Reproduced with permission.[141] Copyright 2019, China Science Publishing. Lithography and 3D printing images. Reproduced with permission.[49] Copyright 2019, Wiley-VCH.

electrolytes. These involve facile preparation processes and display high ionic conductivity and favorable mechanical flexibility without the risk of leakage. In particular, the aqueous gel polymer electrolytes are highly compatible for NIMEESDs as far as safety is concerned, but suffer from the narrow electrochemical window due to the water decomposition. The regenerative water-in-salt electrolytes with large voltage window provide a novel method to fabricate high-voltage aqueous NIMBs and NIMCs with high energy density. This fills the gap between high voltage and aqueous electrolyte by suppressing the hydrogen evolution and oxygen evolution reaction, and decreasing the amount of free water. However, the fluorine-containing electrolytes still take up a large proportion in current NIBs, thus developing the cost-efficient and environment-friendly Na salts is urgent for flexible and wearable devices. In the face of the plentiful electrochemical active materials, it is the ultimate goal to customize NIMEESDs on the basis of required performance; thus, designing high-performance materials by theoretical simulation can make great contribution to fabricating devices in experiments. The era of big data should be considered to establish material database between electrodes and electrolytes.

Second, device configurations and geometric structures of NIMEESDs display discrepant electrolyte ions diffusion behavior and energy output, becoming the key roles in high-energy and high-power NIMEESDs. For 2D stacked NIMCs and NIMBs, the sandwich configuration confines the Na ions diffusion pathways just in vertical direction with complex interfaces between substrate, current collector, cathode, separator/electrolyte, and anode. Thus, high-performance NIMEESDs with high mass loading of electrochemical active materials and abridged inactive materials should not only increase electrical conductivity of microelectrodes with robust structure and ionic conductivity of electrolytes, but also optimize the interface with decreased interface resistance. Differently, the 2D in-plane interdigital NIMCs and NIMBs with Na ions multidirection diffusion mechanisms indicate that appropriate electrode finger width and number can attribute to high-power NIMEESDs with optimized ion diffusion pathways. To meet the demand of customizable NIMEESDs, form factors with various shapes (e.g., concentric circles, linear and foldable geometries) should also be optimized for microelectronics. Importantly, the cathode and anode of 2D in-plane NIMEESDs are on the same planar substrate, suggesting that the evolution of both electrodes can be simultaneously detected during sodiation and desodiation process. It is an ideal model system for mechanism study using (quasi) in situ characterization techniques, such as Raman, X-ray diffraction (XRD), infrared spectroscopy, X-ray photoelectron spectroscopy (XPS), atomic force microscopy (AFM), nuclear magnetic resonance (NMR), and so on. The in situ researches not only help explore fundamental understanding of sodiation/desodiation process and the degradation mechanism of cells, but also provide significant outlook and evidence to develop well-designed electrode materials with robust structure and intensive reaction kinetics for high-performance NIMEESDs. To realize high power and energy density of NIMEESDs simultaneously, the employment of 3D microelectrodes with high mass loading of electrochemical active materials and fast ions/electrons transport is inevitable. Compared with 2D configuration NIMCs and NIMBs, 3D NIMEESDs have not been extensively studied in view of their complicated fabrication process while holding great chance for the future microscale energy storage devices with intriguing electrochemical performance. Undoubtedly, the development of current collector with exceptional mechanical stability should keep pace with the planar and flexible 2D and 3D NIMEESDs. Moreover, 1D flexible fiber-type NIMEESDs undoubtedly play a significant role in the coming wearable and portable era. The fiber-shaped NIMBs with coaxial and parallel structures at centimeter scale have been initially developed. However, the twist-type NIMBs depend on the solid-state electrolyte with high ionic conductivity at the surface of twining electrodes. In addition, the fiber-shaped NIMCs with high power output have not been achieved because of the kinetics discrepancy between anode and cathode. Future research should pay more attention on synthesizing novel fiber materials, devoted to improving electrochemical performance on curved interfaces.

Third, developing high-efficiency, scalable, and low-cost microfabrication technologies is urgently needed for high-performance NIMCs and NIMBs. So far, various microfabrication methods have been expertly implemented for microdevices, such as photolithography,[137] laser scribing,[138] electrochemical deposition,[139] microinjection,[140] plasma etching,[12] printing techniques,[141–143] and mask-assisted filtration,[144,145] from which NIMCs and NIMBs stand to profit. Especially, the printing techniques, including screen printing, spray printing, ink-jet printing, and 3D printing, contribute to mass production of NIMEESDs with shape diversity and tailored self-integration devices. Moreover, the areal loading of active materials can be precisely controlled by printing layers and printing methods with thickness range of nanometer to millimeter, which can achieve the tailored electrochemical performance with desired voltage and capacity/capacitance to meet different practical applications. The key challenge of printing process primarily lies in preparation of printable inks for high-performance devices with adequately high resolution. This requires superior dispersion stability of as-prepared inks, tailored rheological properties with suitable viscosity and surface tension for a specific printing method, strong adhesion with printed substrates, and optimized drying dynamics between substrate and as-printed inks without coffee-ring effects. Generally, the cathode materials of NIBs with a large particle size may plug the nozzles of printer, and especially, the particle size in the ink-jet printing should under the value of 500 nm. To achieve better printability of these inks, it is prerequisite to design nanostructured electrode materials for the required inks. In addition to the fundamental printability, the functional inks must simultaneously fulfill excellent electrochemical properties to achieve high-performance NIMCs and NIMBs, which require well-developed bicontinuous ion and electron transport channels in microelectrodes with hierarchical porous nanostructure, thus the controllable drying process of printing films will become the key to ordered porous structure, involving the evaporation of liquid and aggregation of active components. Moreover, the charming printing technologies can not only act on electrode materials, but also perform in printing solid-state electrolytes with reliable mechanical flexibility, in which the decent rheological properties and ionic conductivity should be secure as essential premises. Logically, it is realizable to print encapsulation materials on the as-fabricated NIMEESDs, thus the NIMCs and NIMBs with simple full printing process could realize mass production. It is noted that the printing technologies with tailored trait in structure, property, and performance of NIMEESDs by controllable printing process are able to cater for microdevices with tailorable structures and functions.

Last but not least, to meet the demand of microelectronics and portable devices (e.g., wireless charging, smart sensor, and implantable medical devices), particular attention has to be paid to microsystems with multiple function integration instead of solo MEESDs, including energy harvester, energy storage, and energy consumption. Specifically, the energy harvesters, e.g., solar cells, hydrovoltaic/piezoelectric/thermoelectric/triboelectric generators, can substantially convert renewable energy sources (e.g., solar, water, thermal, mechanical energy) into available electricity with discontinuity, which can be stored in the advanced NIMCs and NIMBs to drive microscale sensors, display screen, and wearable microelectronics. The as-fabricated standalone microsystem with seamless electrical interconnection provides a stable and sustainable power supply to microelectronics and eliminates superfluous energy loss and bulk increase due to the complex external electric circuit between energy supply and energy consumption. However, the incompatibility between emerging microfabrication methods with the conventional semiconductor industry impedes the achievement of versatile all-in-one microdevices. Fortunately, the reliable printing technologies are expected to aid the design of versatile, aesthetic, customized, and miniaturized NIMEESDs to enable integration with desired functional components on one substrate, effectively improving the energy conversion and utilization efficiency. It is worth mentioning that printing methods can also be effectively performed for encapsulation along with the electrode fabrication, ensuring that the as-fabricated microsystem can endure harsh condition and suppress the leakage of liquid electrolyte. Remarkably, the all-in-one integrated devices usually do not allow the reinstallation of the solo devices, thus it is vital to develop effective Na compensation technologies for the limited-life NIMEESDs due to inevitable Na consumption, which can guarantee the long-term stable supply for standalone microsystem. It cannot be neglected that the biocompatibility and toxicological safety of microsystem in living body are considered as the first principle at any design level. Therefore, friendly functional materials and aqueous electrochemical devices should be deemed as ideal candidates for coming integrated systems. With further development of active materials and microfabrication, we believe that well-developed NIMCs and NIMBs with high power and energy density will achieve mass production, cost-effectiveness, and superior modularization, enabling seamless integration with tailored microelectronic devices.

Acknowledgements

J.M. and S.Z. contributed equally to this work. The authors acknowledge the financial support from National Key R&D Program of China (grant nos. 2016YBF0100100 and 2016YFA0200200), National Natural Science Foundation of China (grant nos. 51872283, 21805273, 51925207, 51872277, and U1910210), Liaoning BaiQianWan Talents Program, LiaoNing Revitalization Talents Program (grant no. XLYC1807153), Natural Science Foundation of Liaoning Province, Joint Research Fund Liaoning-Shenyang National Laboratory for Materials Science (grant no. 20180510038), DICP (grant nos. DICP ZZBS201708, DICP ZZBS201802, and DICP I202032), DICP&QIBEBT (grant no. DICP&QIBEBT UN201702), Dalian National Laboratory for Clean Energy (DNL), CAS, DNL Cooperation Fund, CAS (grant nos. DNL180310, DNL180308, DNL201912, and DNL201915), and the Fundamental Research Funds for the Central Universities (grant no. WK2060140026).

Conflict of Interest

The authors declare no conflict of interest.

Keywords

device configurations, integration, reaction mechanisms, sodium ion microbatteries, sodium ion microcapacitors

Received: July 27, 2020

[1] J. A. Rogers, T. Someya, Y. Huang, *Science* **2010**, *327*, 1603.
[2] X. Shi, S. Pei, F. Zhou, W. Ren, H.-M. Cheng, Z.-S. Wu, X. Bao, *Energy Environ. Sci.* **2019**, *12*, 1534.
[3] Y. Kansha, M. Ishizuka, *Energy* **2019**, *180*, 1001.
[4] J. Ni, L. Li, *Adv. Funct. Mater.* **2018**, *28*, 1704880.
[5] Z. Lei, J. Zhang, L. L. Zhang, N. A. Kumar, X. S. Zhao, *Energy Environ. Sci.* **2016**, *9*, 1891.
[6] P. Lian, Y. Dong, Z.-S. Wu, S. Zheng, X. Wang, W. Sen, C. Sun, J. Qin, X. Shi, X. Bao, *Nano Energy* **2017**, *40*, 1.
[7] Y. Dong, Z. S. Wu, S. Zheng, X. Wang, J. Qin, S. Wang, X. Shi, X. Bao, *ACS Nano* **2017**, *11*, 4792.

[8] Y. Dong, S. Zheng, J. Qin, X. Zhao, H. Shi, X. Wang, J. Chen, Z. S. Wu, *ACS Nano* **2018**, *12*, 2381.
[9] Y. L. Ding, P. Kopold, K. Hahn, P. A. van Aken, J. Maier, Y. Yu, *Adv. Mater.* **2016**, *28*, 7774.
[10] S. H. Kim, K. H. Choi, S. J. Cho, S. Choi, S. Park, S. Y. Lee, *Nano Lett.* **2015**, *15*, 5168.
[11] H. Xiao, Z. S. Wu, L. Chen, F. Zhou, S. Zheng, W. Ren, H. M. Cheng, X. Bao, *ACS Nano* **2017**, *11*, 7284.
[12] Z. S. Wu, Y. Zheng, S. Zheng, S. Wang, C. Sun, K. Parvez, T. Ikeda, X. Bao, K. Mullen, X. Feng, *Adv. Mater.* **2017**, *29*, 1602960.
[13] P. Das, X. Shi, Q. Fu, Z. S. Wu, *Adv. Funct. Mater.* **2019**, *30*, 1908758.
[14] P. Zhang, F. Wang, M. Yu, X. Zhuang, X. Feng, *Chem. Soc. Rev.* **2018**, *47*, 7426.
[15] S. Zheng, X. Tang, Z. S. Wu, Y. Z. Tan, S. Wang, C. Sun, H. M. Cheng, X. Bao, *ACS Nano* **2017**, *11*, 2171.
[16] J. Qin, J. Gao, X. Shi, J. Chang, Y. Dong, S. Zheng, X. Wang, L. Feng, Z. S. Wu, *Adv. Funct. Mater.* **2020**, *30*, 1909756.
[17] K.-H. Lee, S.-S. Lee, D. B. Ahn, J. Lee, D. Byun, S.-Y Lee, *Sci. Adv.* **2020**, *6*, eaaz1692.
[18] X. Huang, P. Wu, *Adv. Funct. Mater.* **2020**, *30*, 1910048.
[19] Y. Lin, Y. Gao, Z. Fan, *Adv. Mater.* **2019**, *29*, 1701736.
[20] F. Su, X. Hou, J. Qin, Z. S. Wu, *Batteries Supercaps* **2019**, *3*, 10.
[21] J. Ma, J. Li, R. Guo, H. Xu, F. Shi, L. Dang, Z. Liu, J. Sun, Z. Lei, *J. Power Sources* **2019**, *428*, 124.
[22] L. Liu, H. Zhao, Y. Lei, *InfoMat* **2019**, *1*, 74.
[23] Q. Jiang, Y. Lei, H. Liang, K. Xi, C. Xia, H. N. Alshareef, *Energy Storage Mater.* **2020**, *27*, 78.
[24] S. Ferrari, M. Loveridge, S. D. Beattie, M. Jahn, R. J. Dashwood, R. Bhagat, *J. Power Sources* **2015**, *286*, 25.
[25] R. Salot, S. Martin, S. Oukassi, M. Bedjaoui, J. Ubrig, *Appl. Surf. Sci.* **2009**, *256*, S54.
[26] S. Zheng, Z.-S. Wu, F. Zhou, X. Wang, J. Ma, C. Liu, Y.-B. He, X. Bao, *Nano Energy* **2018**, *51*, 613.
[27] S. Zheng, J. Ma, Z.-S. Wu, F. Zhou, Y.-B. He, F. Kang, H.-M. Cheng, X. Bao, *Energy Environ. Sci.* **2018**, *11*, 2001.
[28] V. Aravindan, J. Gnanaraj, Y.-S. Lee, S. Madhavi, *Chem. Rev.* **2014**, *114*, 11619.
[29] N. Yabuuchi, K. Kubota, M. Dahbi, S. Komaba, *Chem. Rev.* **2014**, *114*, 11636.
[30] S. Zheng, H. Huang, Y. Dong, S. Wang, F. Zhou, J. Qin, C. Sun, Y. Yu, Z.-S. Wu, X. Bao, *Energy Environ. Sci.* **2020**, *13*, 821.
[31] D. Chao, C. Zhu, P. Yang, X. Xia, J. Liu, J. Wang, X. Fan, S. V. Savilov, J. Lin, H. J. Fan, Z. X. Shen, *Nat. Commun.* **2016**, *7*, 12122.
[32] Q. Li, S. Guo, K. Zhu, K. Jiang, X. Zhang, P. He, H. Zhou, *Adv. Energy Mater.* **2017**, *7*, 1700361.
[33] M. Okoshi, Y. Yamada, A. Yamada, H. Nakai, *J. Electrochem. Soc.* **2013**, *160*, A2160.
[34] P. Zhang, Y. Li, G. Wang, F. Wang, S. Yang, F. Zhu, X. Zhuang, O. G. Schmidt, X. Feng, *Adv. Mater.* **2019**, *31*, e1806005.
[35] T. Hosaka, K. Kubota, A. S. Hameed, S. Komaba, *Chem. Rev.* **2020**, *120*, 6358.
[36] J. Y. Hwang, S. T. Myung, Y. K. Sun, *Chem. Soc. Rev.* **2017**, *46*, 3529.
[37] Y. You, X.-L. Wu, Y.-X. Yin, Y.-G. Guo, *Energy Environ. Sci.* **2014**, *7*, 1643.
[38] Y. Wu, Y. Yu, *Energy Storage Mater.* **2019**, *16*, 323.
[39] Y. Yao, Z. Wei, H. Wang, H. Huang, Y. Jiang, X. Wu, X. Yao, Z. S. Wu, Y. Yu, *Adv. Energy Mater.* **2020**, *10*, 1903698.
[40] S. Zheng, S. Wang, Y. Dong, F. Zhou, J. Qin, X. Wang, F. Su, C. Sun, Z. S. Wu, H. M. Cheng, X. Bao, *Adv. Sci.* **2019**, *6*, 1902147.
[41] S. Guo, Q. Li, P. Liu, M. Chen, H. Zhou, *Nat. Commun.* **2017**, *8*, 135.
[42] J. Deng, W.-B. Luo, X. Lu, Q. Yao, Z. Wang, H.-K. Liu, H. Zhou, S.-X. Dou, *Adv. Energy Mater.* **2018**, *8*, 1701610.
[43] F. Klein, B. Jache, A. Bhide, P. Adelhelm, *Phys. Chem. Chem. Phys.* **2013**, *15*, 15876.
[44] F. Ming, H. Liang, Y. Lei, W. Zhang, H. N. Alshareef, *Nano Energy* **2018**, *53*, 11.
[45] H. Tan, D. Chen, X. Rui, Y. Yu, *Adv. Funct. Mater.* **2019**, *29*, 1808745.
[46] Y. Liu, Q. Liu, A. Zhang, J. Cai, X. Cao, Z. Li, P. D. Asimow, C. Zhou, *ACS Nano* **2018**, *12*, 8323.
[47] D. Cericola, P. Novák, A. Wokaun, R. Kötz, *J. Power Sources* **2011**, *196*, 10305.
[48] M. Beidaghi, Y. Gogotsi, *Energy Environ. Sci.* **2014**, *7*, 867.
[49] S. Zheng, X. Shi, P. Das, Z. S. Wu, X. Bao, *Adv. Mater.* **2019**, *31*, e1900583.
[50] C. Deng, S. Zhang, H. Wang, G. Zhang, *Nano Energy* **2018**, *49*, 419.
[51] F. Mo, G. Liang, Z. Huang, H. Li, D. Wang, C. Zhi, *Adv. Mater.* **2020**, *32*, e1902151.
[52] H. Li, Z. Liu, G. Liang, Y. Huang, Y. Huang, M. Zhu, Z. Pei, Q. Xue, Z. Tang, Y. Wang, B. Li, C. Zhi, *ACS Nano* **2018**, *12*, 3140.
[53] K. Jost, D. P. Durkin, L. M. Haverhals, E. K. Brown, M. Langenstein, H. C. De Long, P. C. Trulove, Y. Gogotsi, G. Dion, *Adv. Energy Mater.* **2015**, *5*, 1401286.
[54] J. Fei, Y. Cui, J. Li, Z. Xu, J. Yang, R. Wang, Y. Cheng, J. Hang, *Chem. Commun.* **2017**, *53*, 13165.
[55] X. Xie, T. Makaryan, M. Zhao, K. L. Van Aken, Y. Gogotsi, G. Wang, *Adv. Energy Mater.* **2016**, *6*, 1502161.
[56] C. Bommier, T. W. Surta, M. Dolgos, X. Ji, *Nano Lett.* **2015**, *15*, 5888.
[57] J. Ding, H. Wang, Z. Li, A. Kohandehghan, K. Cui, Z. Xu, B. Zahiri, X. Tan, E. M. Lotfabad, B. C. Olsen, D. Mitlin, *ACS Nano* **2013**, *7*, 11004.
[58] H. Yang, R. Xu, Y. Yu, *Energy Storage Mater.* **2019**, *22*, 105.
[59] N. Wang, X. Xu, T. Liao, Y. Du, Z. Bai, S. Dou, *Adv. Mater.* **2018**, *30*, e1804157.
[60] S. Chen, Y. Pang, J. Liang, S. Ding, *J. Mater. Chem. A* **2018**, *6*, 13164.
[61] M. A. Tsiamtsouri, P. K. Allan, A. J. Pell, J. M. Stratford, G. Kim, R. N. Kerber, P. C. M. M. Magusin, D. A. Jefferson, C. P. Grey, *Chem. Mater.* **2018**, *30*, 1505.
[62] S. Anwer, Y. Huang, J. Liu, J. Liu, M. Xu, Z. Wang, R. Chen, J. Zhang, F. Wu, *ACS Appl. Mater. Interfaces* **2017**, *9*, 11669.
[63] Z. Yang, G. Li, J. Sun, L. Xie, Y. Jiang, Y. Huang, S. Chen, *Energy Storage Mater.* **2020**, *25*, 724.
[64] Y. You, H. R. Yao, S. Xin, Y. X. Yin, T. T. Zuo, C. P. Yang, Y. G. Guo, Y. Cui, L. J. Wan, J. B. Goodenough, *Adv. Mater.* **2016**, *28*, 7243.
[65] Y. Yue, A. J. Binder, B. Guo, Z. Zhang, Z. A. Qiao, C. Tian, S. Dai, *Angew. Chem. Int. Ed.* **2014**, *53*, 3134.
[66] L. S. Plashnitsa, E. Kobayashi, Y. Noguchi, S. Okada, J.-i. Yamaki, *J. Electrochem. Soc.* **2010**, *157*, A536.
[67] Q. Liu, X. Meng, Z. Wei, D. Wang, Y. Gao, Y. Wei, F. Du, G. Chen, *ACS Appl. Mater. Interfaces* **2016**, *8*, 31709.
[68] J. Z. Guo, P. F. Wang, X. L. Wu, X. H. Zhang, Q. Yan, H. Chen, J. P. Zhang, Y. G. Guo, *Adv. Mater.* **2017**, *29*, 1701968.
[69] S. Li, Y. Dong, L. Xu, X. Xu, L. He, L. Mai, *Adv. Mater.* **2014**, *26*, 3545.
[70] Y. Jiang, H. Zhang, H. Yang, Z. Qi, Y. Yu, *Nanoscale* **2017**, *9*, 6048.
[71] F. Liu, X. Cheng, R. Xu, Y. Wu, Y. Jiang, Y. Yu, *Adv. Funct. Mater.* **2018**, *28*, 1800394.
[72] D. Chen, L. Peng, Y. Yuan, Y. Zhu, Z. Fang, C. Yan, G. Chen, R. Shahbazian-Yassar, J. Lu, K. Amine, G. Yu, *Nano Lett.* **2017**, *17*, 3907.
[73] J. Mei, T. Liao, G. A. Ayoko, Z. Sun, *ACS Appl. Mater. Interfaces* **2019**, *11*, 28205.
[74] J. Mei, T. Liao, Z. Sun, *J. Energy Chem.* **2018**, *27*, 117.
[75] Y. Xu, M. Zhou, Y. Lei, *Adv. Energy Mater.* **2016**, *6*, 1502514.
[76] J. Tang, S. Ni, Q. Chen, W. Han, X. Yang, L. Zhang, *Mater. Lett.* **2017**, *195*, 127.
[77] F. Li, J. Ma, H. Ren, H. Wang, G. Wang, *Mater. Lett.* **2017**, *206*, 132.
[78] Y. Liu, X.-Y. Yu, Y. Fang, X. Zhu, J. Bao, X. Zhou, X. W. Lou, *Joule* **2018**, *2*, 725.

[79] C. Wu, P. Kopold, P. A. van Aken, J. Maier, Y. Yu, *Adv. Mater.* **2017**, *29*, 1604015.
[80] X. Ge, Z. Li, L. Yin, *Nano Energy* **2017**, *32*, 117.
[81] Q. Lin, J. Zhang, D. Kong, T. Cao, S.-W. Zhang, X. Chen, Y. Tao, W. Lv, F. Kang, Q.-H. Yang, *Adv. Energy Mater.* **2019**, *9*, 1803078.
[82] C. Wu, S. X. Dou, Y. Yu, *Small* **2018**, *14*, e1703671.
[83] Y. Dong, W. Shi, P. Lu, J. Qin, S. Zheng, B. Zhang, X. Bao, Z.-S. Wu, *J. Mater. Chem. A* **2018**, *6*, 14324.
[84] J. Ni, Y. Jiang, F. Wu, J. Maier, Y. Yu, L. Li, *Adv. Funct. Mater.* **2018**, *28*, 1707179.
[85] X. Li, A. L. Hector, J. R. Owen, *J. Phys. Chem. C* **2014**, *118*, 29568.
[86] H. C. Yu, C. Ling, J. Bhattacharya, J. C. Thomas, K. Thornton, A. Van der Ven, *Energy Environ. Sci.* **2014**, *7*, 1760.
[87] C. Zhu, P. Kopold, P. A. van Aken, J. Maier, Y. Yu, *Adv. Mater.* **2016**, *28*, 2409.
[88] S. Huang, M. Wang, P. Jia, B. Wang, J. Zhang, Y. Zhao, *Energy Storage Mater.* **2019**, *20*, 225.
[89] W. Chen, X. Zhang, L. Mi, C. Liu, J. Zhang, S. Cui, X. Feng, Y. Cao, C. Shen, *Adv. Mater.* **2019**, *31*, e1806664.
[90] Y. Liu, Y. Yang, X. Wang, Y. Dong, Y. Tang, Z. Yu, Z. Zhao, J. Qiu, *ACS Appl. Mater. Interfaces* **2017**, *9*, 15484.
[91] M. S. Balogun, Y. Luo, F. Lyu, F. Wang, H. Yang, H. Li, C. Liang, M. Huang, Y. Huang, Y. Tong, *ACS Appl. Mater. Interfaces* **2016**, *8*, 9733.
[92] J. Zhang, K. Zhang, J. Yang, G.-H. Lee, J. Shin, V. Wing-hei Lau, Y.-M. Kang, *Adv. Energy Mater.* **2018**, *8*, 1800283.
[93] Y. Wang, D. Kong, W. Shi, B. Liu, G. J. Sim, Q. Ge, H. Y. Yang, *Adv. Energy Mater.* **2016**, *6*, 1601057.
[94] Y. Jiang, M. Hu, D. Zhang, T. Yuan, W. Sun, B. Xu, M. Yan, *Nano Energy* **2014**, *5*, 60.
[95] Y. Zhang, Y. V. Lim, S. Huang, M. E. Pam, Y. Wang, L. K. Ang, Y. Shi, H. Y. Yang, *Small* **2018**, *14*, e1800898.
[96] M. Fan, Y. Chen, Y. Xie, T. Yang, X. Shen, N. Xu, H. Yu, C. Yan, *Adv. Funct. Mater.* **2016**, *26*, 5019.
[97] S. Yuan, X. L. Huang, D. L. Ma, H. G. Wang, F. Z. Meng, X. B. Zhang, *Adv. Mater.* **2014**, *26*, 2273.
[98] J. Qian, Y. Chen, L. Wu, Y. Cao, X. Ai, H. Yang, *Chem. Commun.* **2012**, *48*, 7070.
[99] L. D. Ellis, T. D. Hatchard, M. N. Obrovac, *J. Electrochem. Soc.* **2012**, *159*, A1801.
[100] Y. Xu, E. Swaans, S. Basak, H. W. Zandbergen, D. M. Borsa, F. M. Mulder, *Adv. Energy Mater.* **2016**, *6*, 1501436.
[101] Y. Fu, Q. Wei, G. Zhang, S. Sun, *Adv. Energy Mater.* **2018**, *8*, 1703058.
[102] Y. Wu, Z. Liu, X. Zhong, X. Cheng, Z. Fan, Y. Yu, *Small* **2018**, *14*, e1703472.
[103] J. W. Wang, X. H. Liu, S. X. Mao, J. Y. Huang, *Nano Lett.* **2012**, *12*, 5897.
[104] K. P. S. S. Hembram, H. Jung, B. C. Yeo, S. J. Pai, S. Kim, K.-R. Lee, S. S. Han, *J. Phys. Chem. C* **2015**, *119*, 15041.
[105] H. Yang, R. Xu, Y. Yao, S. Ye, X. Zhou, Y. Yu, *Adv. Funct. Mater.* **2019**, *29*, 1809195.
[106] X. Sun, W. Li, X. Zhong, Y. Yu, *Energy Storage Mater.* **2017**, *9*, 112.
[107] Y. Liu, N. Zhang, L. Jiao, J. Chen, *Adv. Mater.* **2015**, *27*, 6702.
[108] H. Gao, T. Zhou, Y. Zheng, Y. Liu, J. Chen, H. Liu, Z. Guo, *Adv. Energy Mater.* **2016**, *6*, 1601037.
[109] W. Tian, S. Zhang, C. Huo, D. Zhu, Q. Li, L. Wang, X. Ren, L. Xie, S. Guo, P. K. Chu, H. Zeng, K. Huo, *ACS Nano* **2018**, *12*, 1887.
[110] J. Zhu, D. Deng, *J. Phys. Chem. C* **2015**, *119*, 21323.
[111] C. Yang, X. Ou, X. Xiong, F. Zheng, R. Hu, Y. Chen, M. Liu, K. Huang, *Energy Environ. Sci.* **2017**, *10*, 107.
[112] J. Chen, X. Fan, X. Ji, T. Gao, S. Hou, X. Zhou, L. Wang, F. Wang, C. Yang, L. Chen, C. Wang, *Energy Environ. Sci.* **2018**, *11*, 1218.
[113] J.-Y. Liao, A. Manthiram, *Nano Energy* **2015**, *18*, 20.
[114] J. Mei, T. Liao, J. Liang, Y. Qiao, S. X. Dou, Z. Sun, *Adv. Energy Mater.* **2019**, *10*, 1901997.
[115] A. Hayashi, K. Noi, A. Sakuda, M. Tatsumisago, *Nat. Commun.* **2012**, *3*, 856.
[116] W. Zhang, Y. Liu, C. Chen, Z. Li, Y. Huang, X. Hu, *Small* **2015**, *11*, 3822.
[117] S. Dong, L. Shen, H. Li, G. Pang, H. Dou, X. Zhang, *Adv. Funct. Mater.* **2016**, *26*, 3703.
[118] Z. Guo, Y. Zhao, Y. Ding, X. Dong, L. Chen, J. Cao, C. Wang, Y. Xia, H. Peng, Y. Wang, *Chem* **2017**, *3*, 348.
[119] J. Ni, S. Fu, Y. Yuan, L. Ma, Y. Jiang, L. Li, J. Lu, *Adv. Mater.* **2018**, *30*, 1704337.
[120] G. Zhang, F. Geng, T. Zhao, F. Zhou, N. Zhang, S. Zhang, C. Deng, *ACS Appl. Mater. Interfaces* **2018**, *10*, 42268.
[121] L.-F. Que, F.-D. Yu, K.-W. He, Z.-B. Wang, D.-M. Gu, *Chem. Mater.* **2017**, *29*, 9133.
[122] M. Cao, L. Gao, X. Lv, Y. Shen, *J. Power Sources* **2017**, *350*, 87.
[123] D. Chao, C.-H. M. Lai, P. Liang, Q. Wei, Y.-S. Wang, C. R. Zhu, G. Deng, V. V. T. Doan-Nguyen, J. Lin, L. Mai, H. J. Fan, B. Dunn, Z. X. Shen, *Adv. Energy Mater.* **2018**, *8*, 1800058.
[124] M. Liao, L. Ye, Y. Zhang, T. Chen, H. Peng, *Adv. Electron. Mater.* **2019**, *5*, 1800456.
[125] Y. H. Zhu, S. Yuan, D. Bao, Y. B. Yin, H. X. Zhong, X. B. Zhang, J. M. Yan, Q. Jiang, *Adv. Mater.* **2017**, *29*, 1603719.
[126] Q. Chen, S. Sun, T. Zhai, M. Yang, X. Zhao, H. Xia, *Adv. Energy Mater.* **2018**, *8*, 1800054.
[127] Y. Wang, D. Kong, S. Huang, Y. Shi, M. Ding, Y. Von Lim, T. Xu, F. Chen, X. Li, H. Y. Yang, *J. Mater. Chem. A* **2018**, *6*, 10813.
[128] J. Qin, P. Das, S. Zheng, Z.-S. Wu, *APL Mater.* **2019**, *7*, 090902.
[129] P. Zhang, L. Wang, F. Wang, D. Tan, G. Wang, S. Yang, M. Yu, J. Zhang, X. Feng, *Batteries Supercaps* **2019**, *2*, 918.
[130] T. Jin, Y. Liu, Y. Li, K. Cao, X. Wang, L. Jiao, *Adv. Energy Mater.* **2017**, *7*, 1700087.
[131] X. Zhao, Y. Zhang, Y. Wang, H. Wei, *Batteries Supercaps* **2019**, *2*, 1.
[132] R.-M. Gao, Z.-J. Zheng, P.-F. Wang, C.-Y. Wang, H. Ye, F.-F. Cao, *Energy Storage Mater.* **2020**, *30*, 9.
[133] H. Li, X. Zhang, Z. Zhao, Z. Hu, X. Liu, G. Yu, *Energy Storage Mater.* **2020**, *26*, 83.
[134] Y. Chen, X. Li, K. Park, W. Lu, C. Wang, W. Xue, F. Yang, J. Zhou, L. Suo, T. Lin, H. Huang, J. Li, J. B. Goodenough, *Chem* **2017**, *3*, 152.
[135] W. Li, S. Hu, X. Luo, Z. Li, X. Sun, M. Li, F. Liu, Y. Yu, *Adv. Mater.* **2017**, *29*, 1605820.
[136] M. S. Kim, W. J. Lee, S. M. Paek, J. K. Park, *ACS Appl. Mater. Interfaces* **2018**, *10*, 32102.
[137] J. Chmiola, C. Largeot, P.-L. Taberna, P. Simon, Y. Gogotsi, *Science* **2010**, *328*, 480.
[138] M. F. El-Kady, R. B. Kaner, *Nat. Commun.* **2013**, *4*, 1475.
[139] L. Li, J. Zhang, Z. Peng, Y. Li, C. Gao, Y. Ji, R. Ye, N. D. Kim, Q. Zhong, Y. Yang, H. Fei, G. Ruan, J. M. Tour, *Adv. Mater.* **2016**, *28*, 838.
[140] K. Yoshima, H. Munakata, K. Kanamura, *J. Power Sources* **2012**, *208*, 404.
[141] X. Wang, S. Zheng, F. Zhou, J. Qin, X. Shi, S. Wang, C. Sun, X. Bao, Z.-S. Wu, *Natl. Sci. Rev.* **2019**, *6*, 1.
[142] N. Singh, C. Galande, A. Miranda, A. Mathkar, W. Gao, A. L. Reddy, A. Vlad, P. M. Ajayan, *Sci. Rep.* **2012**, *2*, 481.
[143] T. S. Wei, B. Y. Ahn, J. Grotto, J. A. Lewis, *Adv. Mater.* **2018**, *30*, e1703027.
[144] H. Xiao, Z.-S. Wu, F. Zhou, S. Zheng, D. Sui, Y. Chen, X. Bao, *Energy Storage Mater.* **2018**, *13*, 233.

[145] X. Wang, Y. Li, S. Wang, F. Zhou, P. Das, C. Sun, S. Zheng, Z. S. Wu, *Adv. Energy Mater.* **2020**, *10*, 2000081.
[146] Y. Marcus, *Chem. Rev.* **1988**, *88*, 1475.
[147] E. R. Nightingale, *J. Phys. Chem. C* **1959**, *63*, 1381.
[148] Y. Matsuda, H. Nakashima, M. Morita, Y. Takasu, *J. Electrochem. Soc.* **1981**, *128*, 2552.
[149] X. Cheng, D. Li, Y. Wu, R. Xu, Y. Yu, *J. Mater. Chem. A* **2019**, *7*, 4913.

Jiaxin Ma is currently a Ph.D. candidate at Dalian Institute of Chemical Physics (DICP), Chinese Academy of Sciences (CAS), under the supervision of Professor Zhong-Shuai Wu. He received his B.S. from Shaanxi Normal University in 2018. His current research is focused on 2D energy materials and printable microscale electrochemical energy storage devices.

Yan Yu is a professor of material science at the University of Science and Technology of China (USTC). She received her Ph.D. in material science at USTC in 2006. From 2007 to 2008, she worked as a postdoctoral researcher at Florida International University. She worked at the Max Planck Institute for Solid-State Research in Stuttgart, Germany. Her current research interests mainly include the design of novel nanomaterials for clean energy, especially for batteries and the fundamental science of energy storage systems.

Zhong-Shuai Wu received his Ph.D. from the Institute for Metal Research, CAS, in 2011 and worked as a postdoctoral fellow at the Max Planck Institute for Polymer Research in Mainz, Germany, from 2011 to 2015. Subsequently, he became a full professor and group leader of 2D materials chemistry & energy applications at DICP, CAS, and was promoted in 2018 as a DICP Chair Professor. Currently, His research interests include graphene and 2D materials, surface- and nanoelectrochemistry, microscale electrochemical energy storage devices, supercapacitors, batteries, and catalysts.